MSc Thesis Mechanical Engineering

# Wear and degradation of connector rod-tulip contact in a Medium Voltage Switchgear

Kürşat Kaan Çilingir

**Graduation committee**

Prof.dr.ir. M.B. de Rooij
Dr. T. Mishra
Dr. J. Hazrati Marangalou
ing. G.W. Hendriks

May 29, 2024

Chair of Surface Technology and Tribology
Faculty of Engineering Technology,
Mechanical Engineering,
University of Twente

UNIVERSITY OF TWENTE.

**Abstract**

This master thesis presents the wear and degradation phenomena occurring at the contact interface between the connecting rod and tulip in medium voltage switchgear. It particularly investigates the effects of operational temperatures and the frequency of switching operations on wear and surface degradation in lubricated conditions. The connecting rod and the tulip consist of a copper substrate coated with a layer of silver, 10 $\mu$m thick. To simulate the contact pressure between the connecting rod and tulip within the switchgear, a tribological wear test, using the UMT tribometer, was performed. The experimental setup employed was a cylinder on plate configuration, using the connecting rod as the cylinder and a similarly silver-coated copper plate as the counterbody.

The experimental parameters for this study include velocity, temperature and number of strokes, which represent the parameters of switching. The velocity was set to the fastest switching in the switchgear, at 10 mm/s. Temperature parameters varied from ambient up to the maximum operational temperature of the switchgear, which is 115 °C. The switching frequency examined ranged from daily to yearly, with each sequence conducting a maximum of 1000 strokes.

Before conducting the wear tests, the system was assessed under a boundary lubrication regime. Additionally, surface characterization was performed, including measurements of surface roughness and hardness. These initial values provided a base for comparison with the results obtained after the wear tests.

After the wear tests, the surfaces exhibited material transfer and adhesive wear. The tests under the increasing operating temperature and strokes revealed that the surface roughness parameters, Ra and Rq, decreased by half from their initial untested values, indicating material transfer and surface flattening. Additionally, there was an observed increase in the coating thickness on the connecting rod. Lumps were noted on the surfaces of both the connecting rod and the plate, which are crucial in determining the real contact area and can therefore affect the electrical contact resistance (ECR). It was also noted that the lambda ratio decreased further, suggesting a reduction in lubrication effectiveness.

Based on the results, it can be concluded that adhesive wear is the predominant wear mechanism in the switchgear towards the end of its lifespan.

*Keywords*: Electrical contact, Silver coated copper, Adhesive wear, Connector mechanism

# Contents

# 1 Introduction

When electricity in houses is temporarily out due to problems like overload, the house distribution board, which contains the electrical switches, is inspected and after the problem is resolved, the electricity is restored. Electricity is restored after switching the switches, as shown in figure 1.1a. The circuit breaker's function is to interrupt electrical flow when the current flow increases in a circuit to prevent overheating of wires or damaging the electrical equipment. Figure 1.1b shows a simplified circuit diagram where the breakers interrupting the system as mentioned above [1, 2]. System interruption can occur on various scales, from residential homes to industrial factories, and at different voltage levels indicating that the fundamental principles of the low, medium, and high voltage distribution grids are the same. The global power management company Eaton is an important company in the electrical sector. Their plant in Hengelo is part of the electrical systems and solutions division and produces different types of switchgear.

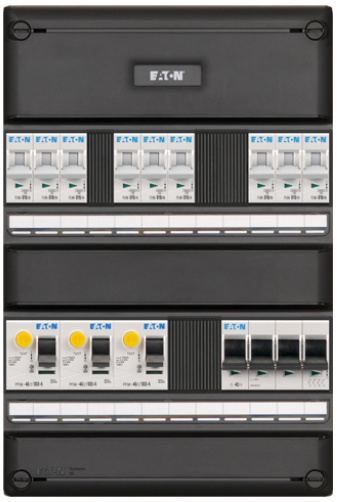

(A) Eaton's house distribution board [3]

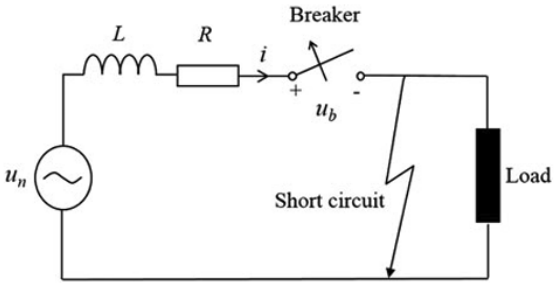


(B) Simplified circuit diagram with a breaker [2]

FIGURE 1.1: Schematic working of the electrical flow

A switchgear is a combination of circuit breakers, switches, and fuses, which automatically interrupt the flow of power to protect, control, and isolate electrical equipment. Moreover, it is used for de-energizing the equipment for maintenance activities and testing to eradicate the defect. It can be classified based on the voltage range it handles: Low voltage (LV) and Medium voltage (MV) and High voltage (HV). The LV switchgear operates at voltages below 1kV, the MV switchgear has a voltage range between 3kV and 36kV. HV switchgear operates at voltages greater than 35kV [3–5].

Maintaining the reliability of the switchgear can be a challenge, as its lifespan can reach 30 to 50 years. Electrical contacts within switchgear components, such as circuit breaker and disconnector, can wear out due to aging. These types of contact face a lot of mechanical stress and forces during the operation time, which slowly wear out the contact surfaces. However, there are several parameters, such as temperature and moisture, that fasten wear processes, which influences the efficiency and safety of the electrical system [6]. Myshkin [7] also confirmed that the main problems that can occur in electrical contacts are tribological phenomena.

According to the Council on Large Electrical Systems (CIGRE), degradation in switchgears built in the early 2000s was dominated by wear. Also, 60% of all the failures on the disconnector was caused by wear [8]. In sliding electrical connectors, like the disconnecter, degradation occurs mainly due to abrasive and adhesive wear [9]. Wear of electrical contacts can have an influence on the surface contact area, which can increase the electrical contact resistance (ECR), that leads to high power loss coupled with thermal stress[10]. However, there is a lack of information on the wear phenomena in lubricated electrical contacts inside switchgears which can affect the ECR.

This research focusses on Eaton's MV switchgear SVS, notable for its modular compact design. It operates across a voltage range of 3.6kV to 24kV and was introduced in 1989. Moreover, the SVS is known for its low maintenance and different kind or amount of panels. Each panel consists of three main components: a circuit breaker, a connector mechanism, and a rail system. Figure 1.2 shows the SVS.

(A) SVS with multiple panels

(B) Modular part of the SVS

FIGURE 1.2: The medium voltage switchgear SVS [3]

## 1.1 Background and motivation

A switchgear has three important tasks: distributing the electrical flow, interrupting the electrical flow and disconnecting to create a safety gap. To ensure the safety of operators

and maintenance personnel, according to IEC 62271-200 [11], the device must be electrically isolated. The system will be completely safe after the circuit breaker disconnects the electrical flow and the disconnector creates an earthed barrier [12].

### 1.1.1 Circuit breaker

Circuit breakers are used to switch and interrupt electrical flow through the circuit and are classified into different types according to the ambient medium in which they operate [5]. Eaton [13] used oil circuit breakers in the past and stopped using oil circuit breakers and replaced them with vacuum circuit breakers, which is also a trend worldwide. Figure 1.3a shows the vacuum interrupter, which is the key component of the vacuum circuit breaker where the contact occurs.

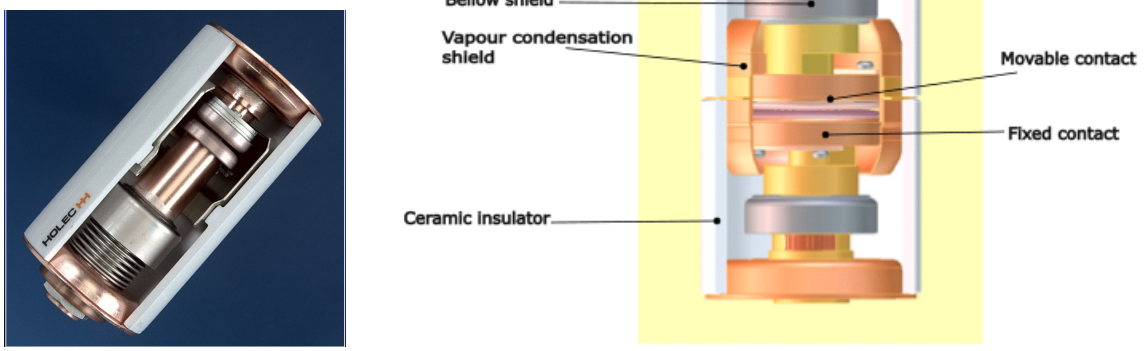


(A) Vacuum interrupter used for the switching of the SVS

(B) Cross section

FIGURE 1.3: Eaton's vacuum interrupter [13]

Figure 1.3b shows the cross section of the vacuum interrupter. The interrupter is insulated by an ceramic insulator and operates within vacuum environment. It consists of a movable and fixed contact, where movement can occur because of the bellows. There are multiple shields to protect components to minimize the contamination that can occur due to vapor.

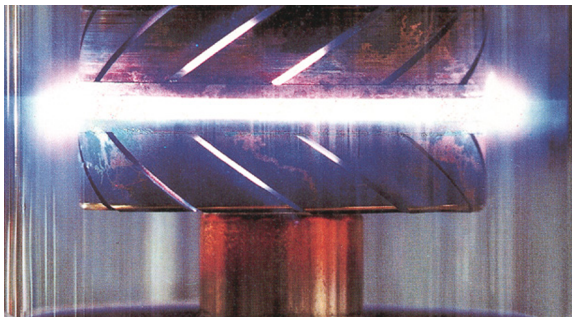

FIGURE 1.4: Diffusive discharge [13]

Figure 1.4 shows the diffusive discharge. During the breaking parallel arcs are spread over the contact area. This means that with high current the arcs are not concentrated in a tiny spot, which helps to protect the contact.

### 1.1.2 Connector mechanism

The safety of the operators can be ensured by using the connector mechanism. This mechanism operates as an extra level of safety to keep the switchgear electrically free. It also the connection between the other SVS modules. The connector mechanism is manually driven and consists of two components: a connecting rod and a tulip. Figure 1.5 shows the schematic of the connector mechanism. The connecting rod can move in the vertical direction and penetrate the tulip. The tulip is compressed with circular spring around its diameter, which keeps the connecting rod inside the tulip after insertion.

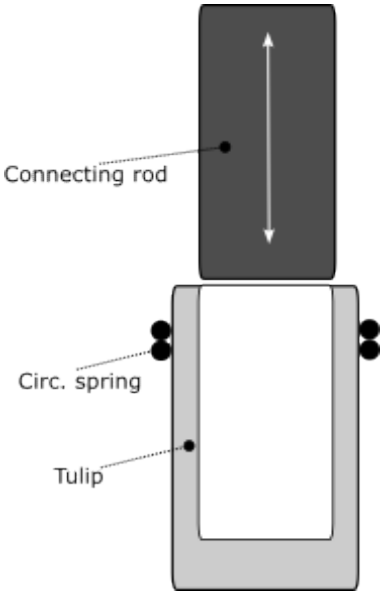


(A) Schematic of the cross section of the components

(B) Connecting rod, tulip and circular spring

FIGURE 1.5: The components of the connector mechanism in a SVS switchgear

The position of the connector mechanism can only be changed when the circuit breaker is in open position. The connector mechanism can have the busbar (service) and earthing position. Figure 1.6a shows that in the busbar position, where the connecting rod is in contact with the tulip, the electricity can flow inside the switchgear, this is called the normal service position. Even after switching, the switchgear remains in the service position. The safety can be created by creating an earthing barrier, which is shown in figure 1.6b. The connecting rod is not in contact with the tulip. As a result the electrical flow through the rail system is also disconnected. This makes the switchgear completely safe for doing maintenance activities.

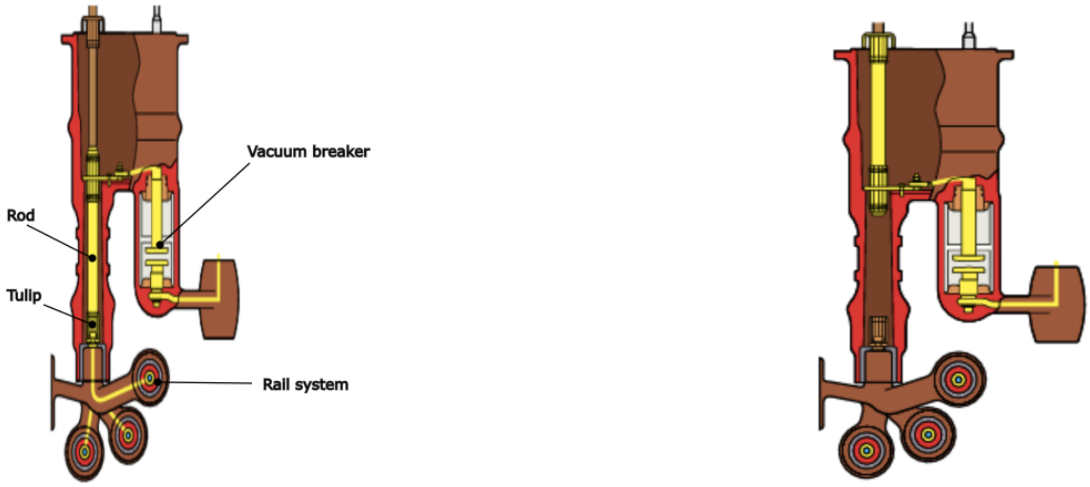


(A) Busbar (B) Earthing

FIGURE 1.6: The position of the connector mechanism after switching the disconnector [3]

### 1.1.3 Operating conditions

Different types of switchgear are operated worldwide, which means that operating conditions can be extreme. The SVS was designed according to IEC 62271-1 [14]. The normal service conditions of the indoor switchgear must not exceed the ambient temperature of 40°C and must not drop below the ambient temperature of -5°C. Furthermore, the standard explains that for the electrical contact silver, tin and nickel contacts can be used. If a silver coating is used for the electric contact, the maximum temperature may not exceed 75K. As a result, the SVS may reach a maximum temperature of of 115°C.

## 1.2 Problem statement

The lifespan of the SVS can be influenced by various external factors. The SVS connector mechanism is capable of switching up to 1,000 times, but the actual frequency of switching is determined by the user, which can range from daily, weekly, monthly and yearly intervals. Consequently, with appropriate use, the SVS could potentially reach a lifespan of up to 40 years. However, variations in temperature during different operating conditions can have an impact on the lifetime of the switchgear, especially on the effectiveness of the electrical contacts of the connector mechanism. In this system, the connecting rod is able to push-in and push-out 1,000 times under standard operating conditions. To minimize friction and ensure smooth operation of the connector mechanism, expensive dielectric lubrication is applied. However, because of external factors, the lubrication can solidify and leak out of the contact, leading to challenges in making or breaking electrical connections, the surfaces of the connecting rod and tulip, which can affect the surface roughness and coating thickness, leading to increased contact resistance of the components.

The scope of this research is to investigate the influence of different factors, such as temperature and operational frequency, on the wear and degradation of the SVS.

## 1.3 Research questions, aims and objectives

The focus of this research will be on the contact and wear of connector mechanism. There are too many critical variables, such as the operating conditions and frequency of switching, which can affect the lifespan of the connector mechanism. These variables are considered critical, since it can have an impact on the lubrication, which can influence the contact resistance of the connecting rod and tulip.

The main research question which stems from the problem statement is:

**"Which wear mechanisms have an impact on the lifetime of the connector mechanism of a medium voltage switchgear under different operating conditions?"**

To answer the research question, the following research questions are listed below:

1. What are the operating and contact conditions of the SVS?
2. How can the connector mechanism of the SVS be mimicked in the test configuration?
3. How can the wear and degradation of the system be measured?

The aim of this research is to design and perform tribological tests to study the effect of operating conditions on the lifetime and wear behavior in a connecting rod-tulip contact.

## 1.4 Literature study

### 1.4.1 Wear phenomena

Wear is a common problem in mechanical systems which can be defined as the removal of material from a surface due to damage and degradation. It occurs when surfaces interact under different circumstances, such as sliding, rolling, or impacting. When two surfaces rub against each other, it causes surface damage, resulting in material transfer or loss. Factors such as sliding speed, temperature, hardness, elastic modulus, load and material can affect the wear. Many of these factors acts simultaneously, leading to a synergistic effect that significantly accelerates the wear rate, resulting in increased failure rates and maintenance costs [15–18].

Adhesive wear, figure 2.7a arises when two interacting surfaces under motion experience loads, temperatures or interfacial adhesion, leading to welding or bonding of material on the surfaces. Surfaces with a protective layer of oxide tend to experience less adhesive wear because they are not as form adhesive bonds over the interface.

On the other hand, abrasive wear occurs when hard particles from another surface scratch the surface of the softer material by rubbing. This process has two forms and are shown in figure 2.7b and 2.7c: two-body, where the hard particles are either components of or are embedded within the counter surface, and three-body, where the particles are free and move between the two interacting surfaces. When a single hard particle slides through a flat surface, it creates a groove[19].

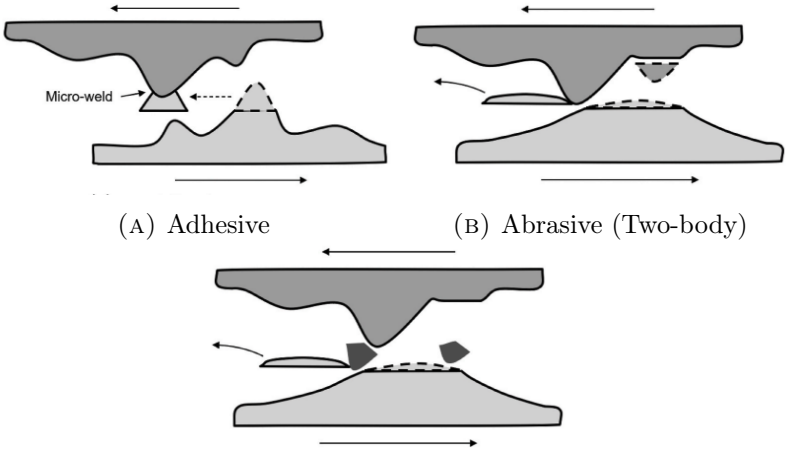


(A) Adhesive (B) Abrasive (Two-body)

(C) Abrasive (Three-body)

FIGURE 1.7: Sliding wear mechanisms [19]

Archard wear equation (1.1) can be used. Archard's equation [20] quantifies the wear volume resulting from the sliding contact between the two surfaces. Parameters are the wear volume (V), wear coefficient (k), applied normal load (N), the sliding distance (s) and the hardness (H). This method can relate the wear volume to the mechanical properties and the operating conditions. Moreover, the Archard's wear law is a simplification, by not taking important parameters into account, such as environmental conditions and lubricants.

$$V = \frac{k \cdot N \cdot s}{H} \tag{1.1}$$

Figure 1.8 shows the evolution of wear in three phases: the running-in, steady-state, and wear-out stages. In the running-in phase, a high wear rate can be observed due to the roughness of the surface, two contacts occur in between the asperities and this is called the real contact. Due to the sliding action, contact points are formed and reduced back to zero as new contact points come into being on different parts of the surface. This cycle repeats until the system transitions to steady state. In the steady state, the nominal contact area is participating. However, some roughness still remains and continues to wear in a constant rate. This indicates the system's adjustment to the load and sliding conditions, leading to a steadier and more predictable pattern of wear. The steady state lasts until the increased friction, and the temperature of worn parts leads to failure. [21].

According to Podgornik [22], adhesive wear occurs through a process known as cold welding, where the particles detach from one contact surface and adhere to the opposing surface. This interaction roughens both contact surfaces. Surface asperities adhere together, forming micro junctions. As these junctions are subjected to load and motion, the asperities may deform, elastically or plastically. Influenced by external variables such as temperature and pressure, the protective interfacial layer between the surfaces can fail, leading to direct metal-to-metal contact. The eventual failure of these junctions through shearing leads to material transfer under cyclic loading results in hardened lumps that changes the actual

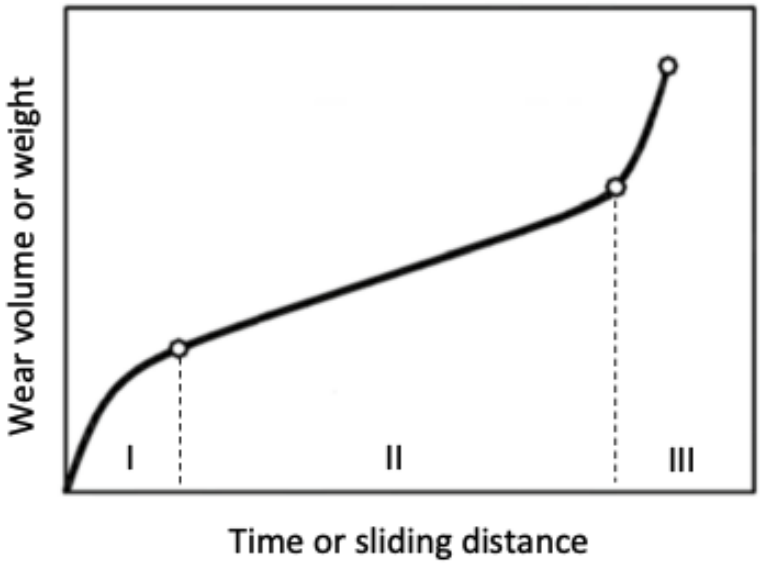


FIGURE 1.8: Typical wear curve with the following phases: (I) Running-in stage, (II) Steady-state wear stage and (III) Wear-out stage [21].

contacting area. The hardened lumps act as abrasive particles, which can damage the surface area. Antler [23] also confirmed that during the adhesive process lumps can be formed on the coating, which can harden and become rougher and act as abrasive particles.

### 1.4.2 Electrical contact resistance

In electrical systems, the electrical contact resistance (ECR) plays a crucial role in the functionality of electrical contacts. An increase in ECR leads to immediate increase in thermal consequences, which affect the performance of the switchgear [24].

Materials with high conductivity are preferred for electrical contacts to ensure efficient current flow with a low ECR. Copper and copper alloys are commonly used in combination with a metallic coating. The reason for using a coating is that the copper oxidize and corrode easily when it is exposed to environmental conditions. Usually soft inert metals such as silver and gold are chosen as the coating. The metals shear more easily, provide large real contact area and an excellent conductivity. Until the silver coating is completely worn through and the copper is not exposed to the environment, the ECR can remain at a low value. Certainly, the thickness of the coating significantly influences the modification of the ECR. As the thickness of the coatings increases, the rate of linear wear diminishes in a non-linear manner. This implies that wear may remain constant over a period, maintaining a steady-state phase. [9, 25, 26].

To ensure the current path of the contact interfaces, roughness plays a crucial role. Even if the surfaces seems smooth to the naked eye, examining them at a microscopic level, it can be observed that the real contact are occurs through the asperities arising from the surface roughness, as shown in figure 1.9. However, these asperities can deform in an elastic-plastic manner due to application of load [27].

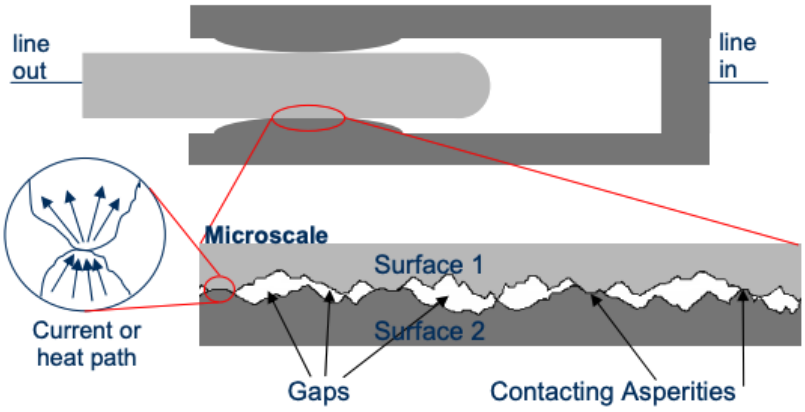


FIGURE 1.9: The real contact area shown in microscale [27]

To calculate the electrical resistance [27] for a wire, equation (1.2) can be used. This formula has the following parameters, which can affect the electrical resistance. The parameters are the electrical resistivity of the material ($\rho$), the length of the material (L) and the real contact area ($A_r$).

$$R = \rho \cdot \frac{L}{A_r} \tag{1.2}$$

The Greenwood and Williamson [28] calculates the real contact area ($A_r$) between rough surfaces by considering the elastic deformation of asperities. Equation (1.3) shows the $N$ is the number of contacting asperities, and $a$ is the contact area of each asperity.

$$A_r = N \times a \tag{1.3}$$

According to Talukder [29] the surface roughness has a critical influence on the ECR. The increase of the surface roughness results in the decrease of the initial contact area. This means that the just the asperities of the contacting bodies are in contact, resulting in an increase of the ECR, as fewer points of contact are available for electrical conduction.

### 1.4.3 Lubrication regimes

Lubrication can also affect the stability of friction and ECR. These special lubricants consists of silver particles, which forms a conductive path to transmit the current between the contact interfaces, which helps to reduce the ECR and COF. Some surfaces consists of textures and have dimples, which act as reservoirs for lubricant, delaying the onset of wear by preserving lubrication on the contact surface even after it breaks down. Further, these dimples can capture wear debris, effectively smoothing the surface [9, 30, 31].

However, the lubrication process of two sliding contacting surfaces is called Elastohydrodynamic Lubrication (EHL). In EHL, non-conformal contacting surfaces under high load deform elastically, allowing the lubricant to increase in viscosity under pressure and maintain a separating film [32]. This reduces wear and friction by combining the elastic deformation of the surfaces with the hydrodynamic properties of the lubricant. There are three different lubricant regimes [33]:

- Full lubrication: The film is sufficiently thick to prevent any metal to metal contact between the surfaces. The film thickness surpasses the combined roughness of the surfaces to ensure smooth motion.
- Mixed lubrication: The surfaces are partially separated by the lubricant film and partially in contact due to the asperities. This regime is considered as the transitional phase between the other two regimes.
- Boundary lubrication: The lubricant film is thinner than the roughness asperities of the surfaces. There is a direct metal to metal contact. Lubrication effectiveness heavily relies on the surface coatings and the lubricants additives.

Figure 1.10 shows the three lubrication regimes given in the Stribeck-curve. It shows how the higher the $\lambda$ ratio is, the more the COF decreases and the more lubrication separates the contacting surfaces by minimizing the metal to metal contact.

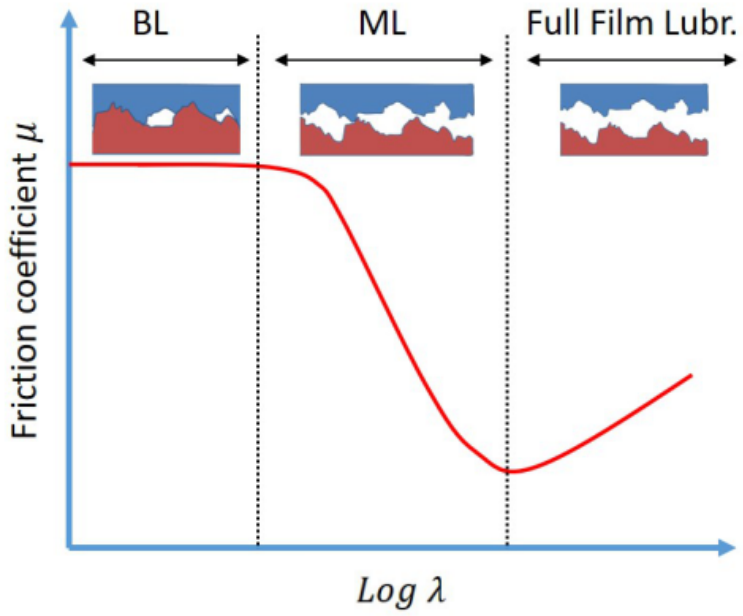


FIGURE 1.10: Stribeck-curve given with the three lubricant regimes: Boundary, mixed and full film lubrication [33]

The $\lambda$ ratio can be calculated by diving the thickness of the lubricant film $h_{\text{film}}$ divided by the effective roughness ($\sigma$) of the surface and is shown in equation (1.4) [34].

$$\lambda = \frac{h_{\text{film}}}{\sigma} = \frac{h_{\text{film}}}{\sqrt{Rq_1^2 + Rq_2^2}} \tag{1.4}$$

The lubrication regime will be a:

- Full film lubrication if $\lambda > 3$.
- Mixed lubrication if $1 < \lambda < 3$.
- Boundary lubrication if $\lambda < 1$.

## 1.5 Research approach

Figure 1.11 shows the approach for this research. It is a combination of numerical analysis and experimental methods. A FEM model of the connector mechanism was made to compute the contact forces, which was validated with contact forces obtained from a performance test using the components inside the SVS. Furthermore, friction tests were performed to define the COF, which was used for the FEM model. The contact force and COF from the performance and friction test and performance test respectively, will be used for determining the operating (contact) parameters for the tribological wear test, which mimics the contact behavior of the connector mechanism.

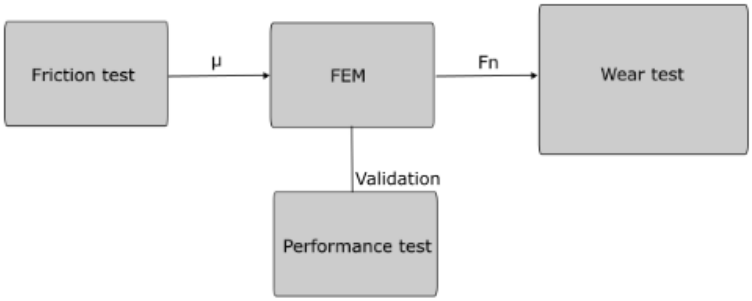


FIGURE 1.11: Flow-chart of the research approach

## 1.6 Thesis outline

This thesis consists of 6 chapters. In the first chapter, all the research related topics were mentioned. Followed with chapter 2 on the contact force analysis, which also defines the parameters for the test configurations. The third chapters mentions the experimental materials and methods that was performed during this thesis. Chapters 4 shows the experimental results. Followed by chapter 5 and chapter 6, which discusses, concludes and recommends regarding to the results.

# 2 Contact force analysis

The procedure for mimicking the contact conditions within the connector mechanism for a tribological setup involves applying contact pressure across both the systems. Figure 2.1 shows the connector mechanism, with its components, which were briefly discussed in section 1.1.2. Performing a contact force analysis is essential for understanding the contact behaviour and establishing the parameters required for the wear testing.

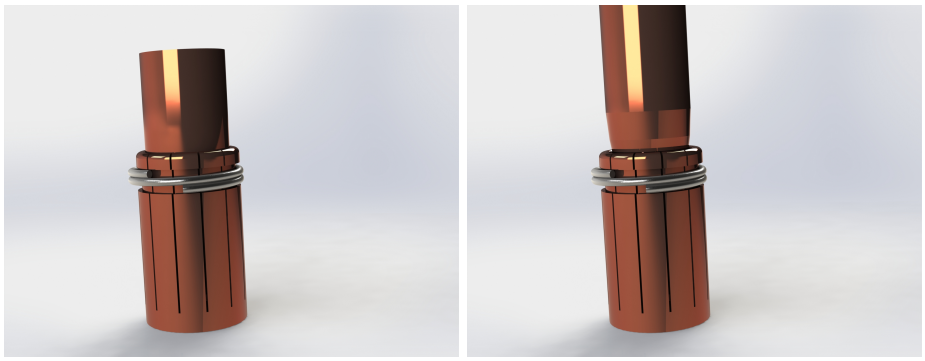

(A) Active (B) In-active

FIGURE 2.1: 3D model of the connector mechanism

By applying Hertzian contact theory [35], the contact area and pressure between two surfaces can be defined. These calculations are initially based on a conforming contact scenario, where the tulip contact section curves into the connecting rod. However, it should be adjusted to a tribological test setup with a non-conformal contact where a cylinder is placed against a flat surface for the wear test, as explained in section 2.3. Therefore, in the contact force analysis, the contact force ($F_L$) that occurs between the cylinder and flat plane in the tribological setup must result in the same contact pressure as that in the contact between the tulip and connecting rod contact due to contact force ($F_c$).

For calculating $F_c$, the penetration force along the sliding direction ($F_y$), as shown in figure 2.3, should be calculated. A Finite Element Method (FEM) model was developed to calculate the $F_y$, and later validated using the performance test explained in section 3.4.

## 2.1 Tribological system

Figure 2.2a shows the tribological system of the connector mechanism and figure 2.2b shows the contacting interfaces of the connecting rods and the tulip which interact during the sliding. It was previously explained that the tulip is a hollow cylindrical tube with an open top face and consists of vertical cantilever beams with gaps resulting in 12

contacting regions with the connecting rod. Therefore, the tribological system replicates a single contact between connecting rod and tulip. The "A" in both figures, the initial contact for the contact surface of the connecting rod and the tapered section at top of the tulip. Following the first contact, the connecting rod slides 20mm in the y-direction. If the radius of curvature of two contacting bodies are in the same direction, resulting in a conformal contact. Upon penetration by the connecting rod, the internal diameter of the tulip increases by 1.2mm. This means that the section of the cantilever beam of the tulip in contact with rod bends by 0.6mm.

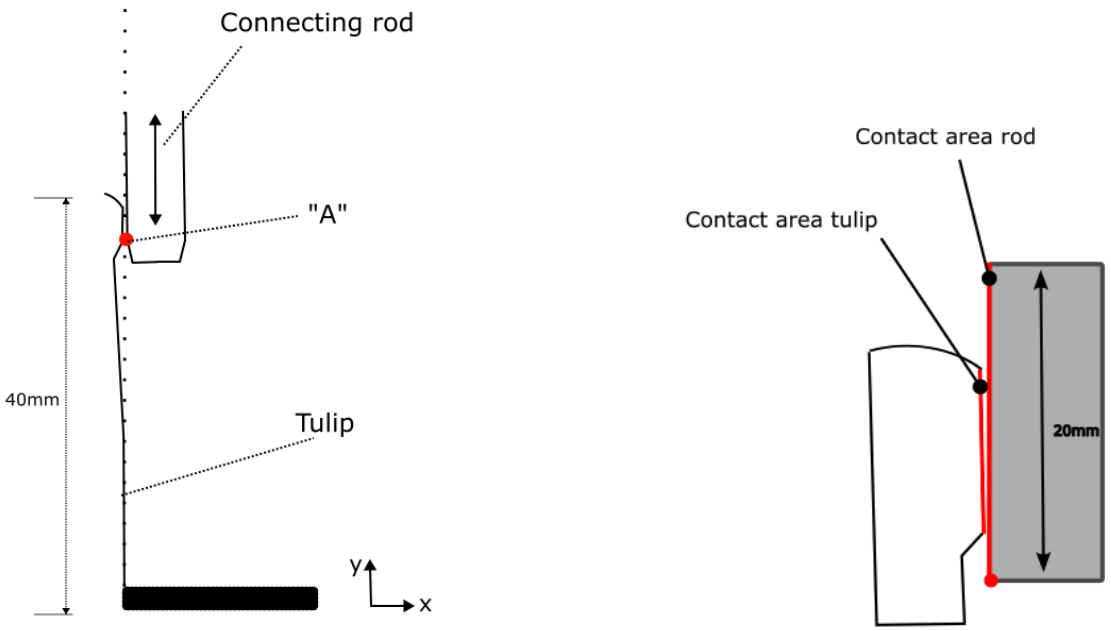


(A) Cross section of the tribological system

(B) Sliding contact between the connecting rod and tulip

FIGURE 2.2: Sliding interfaces of the connector mechanism

Figure 2.3 shows the free body diagram (FBD) of the connecting rod in contact with the section of the tulip. It shows that as a result of the bending, the $F_c$ and the friction force ($F_f$) act at an angle with respect to the x-and-y axis respectively.

The FBD shows that the $F_c$ is dependent of the angle of bending $\theta$ and $F_y$. Equation (2.1) was used to define $\theta$ for one contact point of the vertical cantilever beam. The deflection ($Lx$) was divided by the height of the cantilever ($h$)

$$\tan\theta = \frac{Lx}{h} \tag{2.1}$$

The FBD indicates that the friction force $F_f$ can be determined by applying equation (2.1) using the $F_y$ derived from the FEM model. However, the value of $F_y$ is divided by 12, due to the uniform distribution of the load on the 12 vertical cantilever beams. Consequently, equation 2.2 is formulated as follows:

$$F_f = \left(\frac{F_y}{12}\right) \cdot \cos\theta \tag{2.2}$$

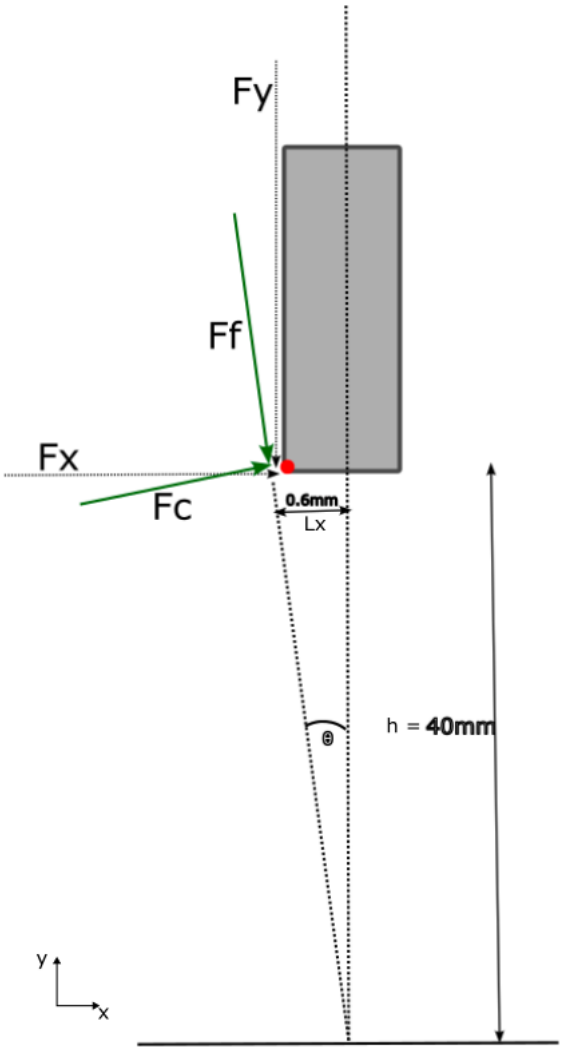


FIGURE 2.3: The free body diagram of the connecting rod during the sliding

The normal contact force between the rod and the tulip $F_c$ can be computed as the ratio of the friction force obtained from equation (2.2) and the coefficient of friction (COF) for the lubricated silver contacts obtained in section 3, using equation (2.3).

$$F_c = \frac{F_f}{\mu} \tag{2.3}$$

By using the following values, equations (2.2) and (2.3) can be calculated:

- $\theta$ is 0.8.
- $F_y$, obtained from section 3.4, is 92.1N. For simplification 90N was used.
- COF obtained from the friction test is 0.15.

The calculated value for $F_c$ is 45N. This value will be used as an input for the calculating the contact load in tribological test setup.

## 2.2 Contact analysis using finite element method

The finite element software ABAQUS is used to simulate the connector mechanism and compute the penetration force. The connector mechanism, shown in figure 2.1, was created using Solidworks (SW) and then transformed into step files to ensure compatibility with ABAQUS.

### 2.2.1 Parts

In analyzing the interaction between circular curved components, such as the connecting rod and the tulip, considering axial symmetry can significantly simplify the computational speed. This approach assumes that the material properties, applied loads, and geometric features are symmetric around the axis of the tulip. This simplification is particularly suitable for the connecting rod, which is fully axi-symmetric. However, the tulip presents a challenge due to the 0.5mm gaps between the cantilever beam sections, which disrupts the continuous symmetry. Using a 2D axisymmetric model will be insufficient to capture the effects of these gaps in terms of load and stress. A 3D modeling approach, with periodic symmetry, can be used to simplify this model. By dividing both parts into symmetric segments, in this case, 30° intervals, the model can capture the symmetry between the connecting rod and tulip contact, including the effects of the gaps, while reducing computational resources compared to modeling the entire 3D structure.

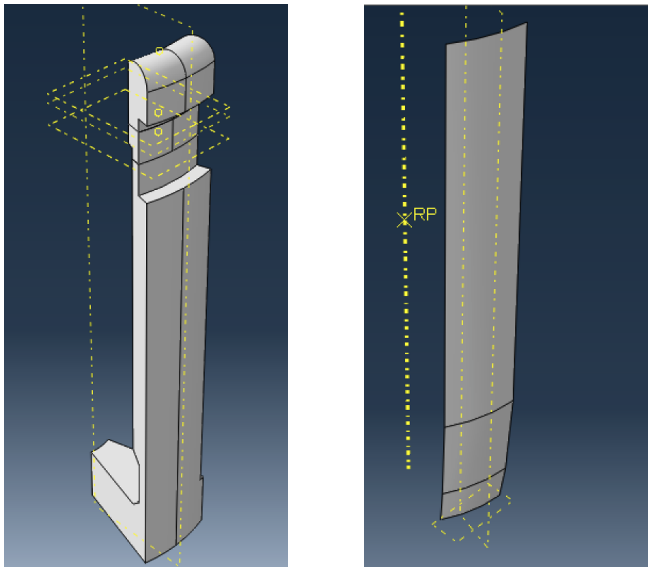


(A) Section of the tulip

(B) Shell element of the connecting rod

FIGURE 2.4: The parts used in the FEM model

In the connector mechanism, the connecting rod behaved as a rigid body, in contrast to the hollow tulip, which behaved as a deformable cantilever. Using the connecting rod as a rigid body was not feasible in ABAQUS due to its small but finite deformation, bulk behavior and coated composition solid. The solution was creating a shell element from the contact surface of the connecting rod, utilizing the inertia values derived from the Solidworks

component. This approach significantly simplifies the meshing process for a shell element as opposed to a solid component. The parts are shown in figure 2.4. Furthermore, $F_y$ acting on the Reference Point (RP), can be computed during the contact when the contacting interfaces of the connecting rod and tulip interacts during the sliding.

### 2.2.2 Meshing

The connecting rod's shell element is a distinct, rigid component, specifically utilizing R3D4 mesh. This choice of a quadrilateral element aims to minimize the size of the element while enhancing accuracy. In the area of contact, a mesh size of 1mm was implemented. For the tulip, which is circular, the C3D15 mesh was selected for the contact area. This decision was made because the 3D model of the tulip is circular, and a wedge element in this context effectively simulates the contact. Similar to the connecting rod, the mesh size at the contact point was maintained at 1mm.

### 2.2.3 Circular spring

The circular spring around the tulip had been neglected in the design parts of the FEM model, but the impact of the circular spring was still considered a boundary condition. In the connector mechanism, the circular spring operates with respect to radial forces. This unique situation allows the circular radially to stretch by as much as 0.3mm. Using the method mentioned in section 2.4, the contact area between the circular spring and the tulip section can be analyzed using the Hertzian contact theory as two cylinders making a crossed contact.

To simplify, given the large diameter of the tulip compared to that of the wire in the circular spring, it is assumed that the spring in contact with the tulip section, acts like a cylinder touching a flat surface. The calculated contact pressure will be checked by using the film pressure test mentioned in section 3.3. The following values: the pressure of the circular spring ($P_{\text{cs}}$) and the contact area of the circular spring ($A_{\mathbf{cs}}$) are used in the FEM model instead of physically modeling the circular spring. Figure 2.5 shows the location of the pressure and the contact area in the tulip section.

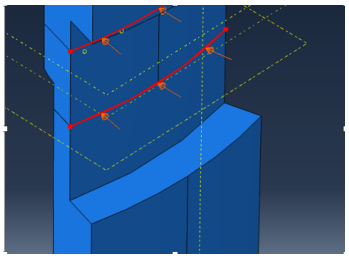

FIGURE 2.5: Spring replacement in the FEM model

In section 4.2 the calculation of the contact pressure in the contact of the circular spring on the tulip is explained. Equations (2.3), (2.4) and (2.5) were used to calculate $P_{\text{cs}}$ and $A_{\text{cs}}$.
The results of these values are:

- $P_{\text{cs}}$ is 16.9 MPa
- $A_{\mathbf{cs}}$ is $2.4 \times 10^{-4}\,\text{mm}^2$

The calculated values are from the analytical model and was used as input for the FEM model to replace the spring.

### 2.2.4 Assembly

The initial position of the base of the connecting rod is $y = 40$mm. From there, it is lowered down to interact with the tulip. There are four boundary conditions used in this model:

1. Circular spring contact pressure and area as explained in section 2.3.2.
2. Encastre: the base of the tulip is fixed. Inside the actual connector mechanism, it is also fixed with a bolt.
3. Sliding: the connecting rod is sliding -20mm in the y-direction
4. Displacement circular spring: the diameter of the tulip decreases by 0.1mm when the spring is fitted around it. Therefore, an x-displacement of 0.05mm at the spring area is included for the modeled section of the tulip.

To enforce contact constraints, the penalty method was used. This method uses virtual springs at the contacting interface and minimize the interpenetration between the connecting rod and the tulip by applying forces that mimic the natural resistance of the materials during interaction. However, due to numerical instability, small step sizes should be used [36]. The step size used for the dynamic implicit was 0.002, which fixed all the errors occurring in the simulation.

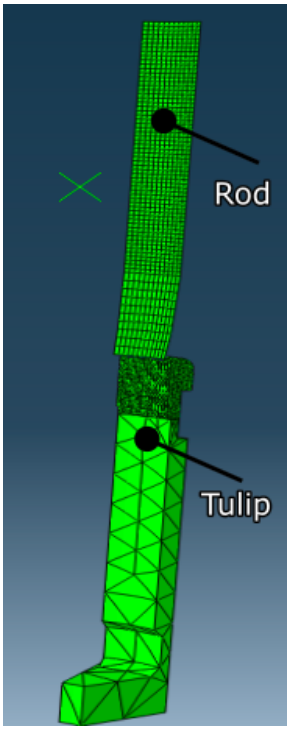


FIGURE 2.6: Meshed assembly of the connector mechanism

## 2.3 Contact analysis using Hertz theory

The contact between the tulip section and the connecting rod and the contact between the circular spring and the tulip can be explained by the Hertzian contact theory, which helps to analyze the stress distribution and the changes in shape in the contact region. The theory is based on the following assumptions: materials are elastic, deformations are small compared to the size of the contacting bodies, and the contact is frictionless. Hertz theory applies to interactions involving spherical, elliptical, and cylindrical contacts. The cylinder is able to interact with another cylinder or a flat surface, as shown in figure 2.7.

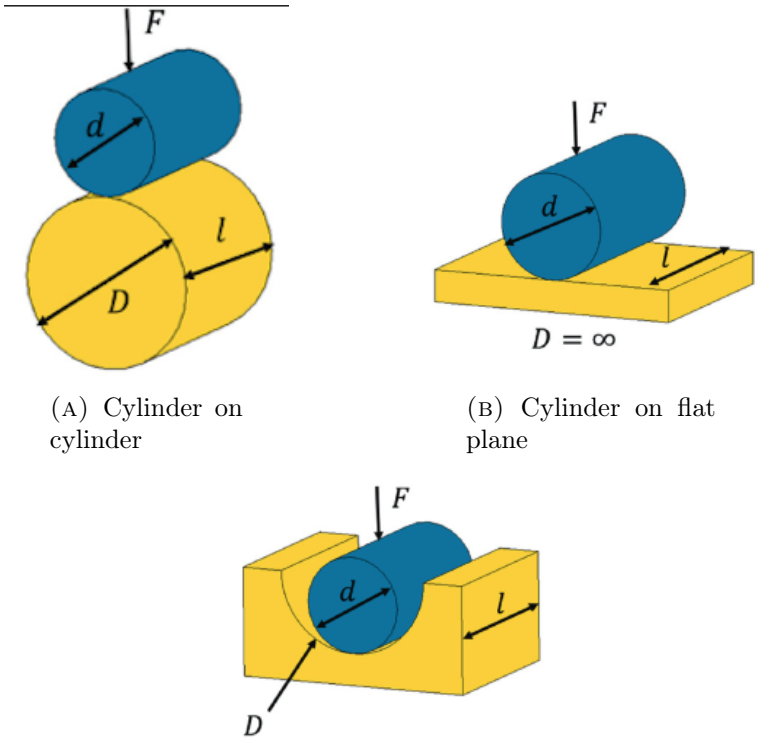


(A) Cylinder on cylinder

(B) Cylinder on flat plane

(C) Cylinder in inner cylinder

FIGURE 2.7: Hertzian contact cylinder scenarios

Previously, it was mentioned that the connector mechanism features a conforming contact, where a convex surface of the cylinder (connecting rod) is in contact with the concave surface of the hollow cylinder (tulip), resulting in Hertzian line contact as shown in figure 2.8a. The top-view shows red areas, the contact width between the two cylinders. Since the cylinder has a length, this area multiples the contact length in line contact. Figure 2.8b shows the configuration of the cylinder on the flat plane, and this configuration was chosen to mimic this specific line contact. This approach simplifies the test setup in comparison to a cylinder in a cylinder conformal contact configuration, which is difficult to mimic in the laboratory.

### 2.3.1 Hertz theory for line contact

The main goal of this section is to calculate the $F_L$, to define the operating parameters for the wear test mentioned in section 4.5. In the Hertzian contact theory, the equivalent Young modulus, in equation (2.4), is used when two elastic bodies with different Young

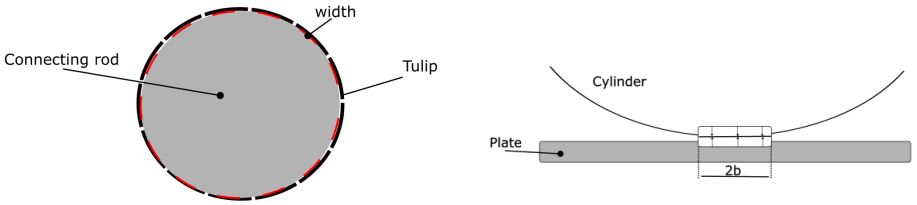


(A) Top-view of the conforming contact

(B) Cylinder on a plane configuration

FIGURE 2.8: Connector mechanism contact configuration in (a) reality and (b) in the tribological lab tester.

modulus, $E_1$ and $E_2$, and Poisson ratio [37], $\nu_1$ and $\nu_2$, contact each other.

$$\frac{1}{E^*} = \frac{1-\nu_1^2}{E_1} + \frac{1-\nu_2^2}{E_2} \tag{2.4}$$

The contact of two curved surfaces, with different radius, can be simplified to the equivalent radius ($R'$) and represents the curvature of the contact interface, see equation (2.5). Convex surfaces has a positive sign for radius and concave surfaces has negative sign for radius. The radius of the plane is infinite.

$$\frac{1}{R'} = \frac{1}{R_1} + \frac{1}{R_2} \tag{2.5}$$

In this scenario a small area of the curved part of cylinder is touching the other cylinder or plane over contact length ($L$). The line contact is rectangular and the half-width ($b$) of this line contact is essential for calculating the maximum pressure as given in equation (2.6).

$$b = 2\sqrt{\frac{FR'}{\pi * L * E^*}} \tag{2.6}$$

The max pressure ($Pmax$) is expressed in equation (2.7).

$$Pmax = \frac{2F}{\pi * L * b} \tag{2.7}$$

The goal is to use the same contact pressure for the wear tests with cylinder on plane configuration as the contact pressure in the connecting rod and tulip contact in cylinder in cylinder contact.

### 2.3.2 Contact between circular spring on tulip

It was earlier explained in section 2.2.2, that for simplification the contact between the tulip section and the circular spring, a cylinder on flat plane configuration is used. Since the radius of the spring wire is very small compared to radius of the tulip. Using equations (2.4-2.7) from section 2.3.3, the pressure on the contact region can be calculated and be implemented in the FEM model.

Figure 2.9 shows the schematic overview of the contact between the circular spring on the tulip contact. There are two cylinders visualized representing two wire (rings) of the circular spring resulting in two contact sections.

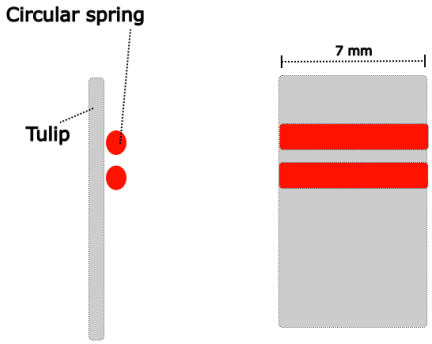


(A) Side-view

(B) Front-view

FIGURE 2.9: Schematic overview: contact between circular spring and tulip

Table 2.1 shows the parameters which were used to calculate the contact pressure of the circular spring on the tulip.

TABLE 2.1: Parameters for contact between tulip and circular spring

| **Description** | **Parameter** | **Value** | **Unit** |
|---|---|---|---|
| Outer Radius (Tulip) | $R_{\text{out}}$ | 30.0 | mm |
| Radius (Spring wire) | $R_{\text{cs}}$ | 1.0 | mm |
| Young's modulus (Circular Spring) | $E_1$ | 200 | GPa |
| Young's modulus (Tulip) | $E_2$ | 115 | GPa |
| Poisson's ratio (Circular Spring) | $\nu_1$ | 0.25 | - |
| Poisson's ratio (Tulip) | $\nu_2$ | 0.35 | - |

To calculate the width of the flat beam ($W$), the circumference of the tulip was determined and the 12 gaps between each beam were subtracted. The calculation is presented in Equation (2.8). These results will also serve as the line contact length of the circular spring ($Lspring$) on the beam.

$$Lspring = \frac{2\pi R_{\text{out}} - (12 \times 0.5)}{12} \tag{2.8}$$

The force opposing the extension of the circular spring was measured, as detailed in the appendix A.1. It was observed that for an extension of 0.2 mm of the diameter of the spring, the radial force required ($F_{cs}$) is 14N. Considering the presence of 12 vertical cantilever beams and two contact points per beam, the total force of 14N was evenly distributed, resulting in $F_{cs}$ being 0.58N per contact point. To calculate the half-width of the circular spring ($b_{cs}$), equations (2.4) and (2.5) were used to calculate E* and R' which were subsequently substituted into equation (2.6). All the obtained values can be substituted into equation (2.7) for calculating the circular spring pressure ($Pcs$). The calculated values are:

- $b_{\text{cs}}$ is $1.7 \times 10^{-4}$ mm
- $P_{\text{cs}}$ is 16.9 MPa

### 2.3.3 Contact between connecting rod and tulip

In this section, the contact pressure $Pcr$ between the connecting rod and the tulip is calculated. The 45N contact force obtained from the FEM analysis and table 2.2 was substituted in equations (2.4-2.7).

TABLE 2.2: Parameters for the connecting rod-tulip contact

| Description | Parameter | Value | Unit |
|---|---|---|---|
| Angle of Vertical Cantilever Beam | $\theta$ | 0.8 | - |
| Young's Modulus (Connecting Rod) | $E_1$ | 115 | GPa |
| Young's Modulus (Tulip) | $E_2$ | 115 | GPa |
| Radius (Connecting Rod) | $R_1$ | 11.0 | mm |
| Inner Radius (Tulip) | $R_2$ | 11.6 | mm |
| Poisson's Ratio (Connecting Rod) | $\nu_1$ | 0.35 | - |
| Poisson's Ratio (Tulip) | $\nu_2$ | 0.35 | - |
| Coefficient of Friction | $\mu$ | 0.15 | - |
| Length (Tulip Contact Section) | $Lt$ | 6.0 | mm |

Given that both the connecting rod and the tulip are composed of both silver coated copper, the Young's modulus of the silver coating measured from nano-indentation, as explained in section 3.2.3. The values for $E_1$ and $E_2$ are each 115 GPa, which can be substituted directly into Equation (2.4). For the purpose of these calculations, it is assumed that the properties of the silver coating on the plate are representative of those of both the connecting rod and the tulip.

Equation (2.5) is rewritten to calculate $R'$ for a conformal contact configuration, making $R_2$ a negative value.

The half-width of the connecting rod-tulip contact ($bcc$) can be calculated by substituting $F_c$, $E^*$, $R'$ and the contact length of the tulip section ($Lt$) in equation (2.6).

In the final step of this calculation, all the calculated results in this section was substituted in equation (2.7) to calculate the $Pcr$.

The following parameters were calculated:

- $b_{\text{cc}}$ is $1.83 \times 10^{-1}$ mm
- $P_{\text{cr}}$ is 27.2 MPa

### 2.3.4 Cylinder on flat plane contact for tribological tests

The contact pressure of 27.2 MPa and the parameters listed in table 2.3 are necessary to calculate the applied normal load required $F_L$ for wear experiments.

TABLE 2.3: Parameters for the connecting rod-plate contact

| **Description** | **Parameter** | **Value** | **Unit** |
|---|---|---|---|
| Young's modulus (Connecting rod) | $E_1$ | 115 | GPa |
| Young's modulus (Plate) | $E_2$ | 115 | GPa |
| Radius (Connecting rod) | $R_1$ | 11.0 | mm |
| Radius (Plate) | $R_2$ | - | - |
| Poisson's ratio (Connecting Rod) | $\nu_1$ | 0.35 | - |
| Poisson's ratio (Plate) | $\nu_2$ | 0.35 | - |
| Coefficient of Friction | $\mu$ | 0.16 | - |
| Length (Plate contact section) | $Lc$ | 20.0 | mm |

Given that both the connecting rod and the plate are composed of both silver coated, the $E^*$ calculated in section 2.3.3 can also be used for this configuration. In the the cylinder on flat plane configuration of the wear test, $R_2$ is set to zero, leading to $R' = R_1$. The length of the sample holder is 20 mm, which determined the contact length ($L_c$) of the cylinder in the plane configuration. Substituting these parameters into equation (2.6) will result in two unknown values, the half width for the wear test configuration ($bw$) and the other value is $F_L$.
To minimize the unknown values into one unknown value, equation (2.6) was substituted into equation (2.7), resulting only in missing the $F_L$ and is shown in equation (2.9).

$$F_L = \frac{Pcr^2 \pi R_1 L_c}{E^*} \tag{2.9}$$

The calculated value of $F_L$ was back substituted in equation (2.6) to define the contact width of the wear configuration. The calculated parameters for the wear test configuration are:

- $b_w$ $2.23 \times 10^{-2}$ mm
- $F_L$ is 8.1N

# 3 Experimental materials and methods

This chapter provides a detailed description of the experimental setup and procedures. Initially, it outlines all the components and test specimens involved in the experiments. This is followed by a thorough characterization of the test specimens surfaces, including measurements of surface thickness, roughness, stiffness, and hardness. Subsequently, a pressure measurement is conducted to estimate the pressure exerted by the circular spring on the tulip. The chapter then details the performance tests and friction tests performed to obtain values crucial for the subsequent wear test.

## 3.1 Experimental materials

### 3.1.1 Test specimens for tensile tester

The connecting rod and tulip was conducted using the Zwick/Roell BT1-FR5.0TN.D30 tensile testing machine. This machine, typically used to measure material tension and ductility, was adapted to simulate the connector mechanism in this setup. Table 3.1 lists the properties of the connecting rod and tulip.

TABLE 3.1: Properties of connector mechanisms components

| **Property** | **Connecting rod** | **Tulip** | **Circular spring** |
|---|---|---|---|
| Material | Cu | Cu | Stainless Steel |
| Diameter (mm) | 22.0 | 22.0 | 18.0 |
| Length (mm) | 400.0 | 150.0 | - |
| Coating Material | Ag | Ag | - |
| Coating Thickness ($\mu$m) | 10 | 10 | - |
| Number of Turns | - | - | 2 |
| Thickness Diameter (mm) | - | - | 2.0 |

The connecting rod (silver-coated copper rod; 22mm diameter, 200mm length) served as the upper test specimen. The connecting rods tip was designed with a taper to mitigate misalignment issues when its penetrating into the tulip. This feature ensures a smoother sliding contact between the two components.

Tulip (silver coated copper; 11 mm inner diameter, 3mm thickness), with geometry comparable with an open-top cylinder, served as the lower test specimen. The tulip is segmented into 12 sections, separated by 0.5mm gaps, allowing for flexibility and compression. A circular ring spring encircles the tulip, applying inward pressure to reduce its diameter by 0.1mm, ensuring the fixed position as soon as the connecting rod is placed inside the

tulip.For all the other tests a plate (silver coated copper; 1mm thickness) was used as the counter body for the connecting rod.

### 3.1.2 Test specimens for Universal Mechanical Tester

For the experiments related to wear and friction, the Universal Mechanical Tester (UMT) from Bruker was used. When the connecting rod slides inside the tulip, they are in contact over a certain area. In the tribological setup, the cylinder on a flat plane was used to mimic the contact pressure of the connector mechanism.

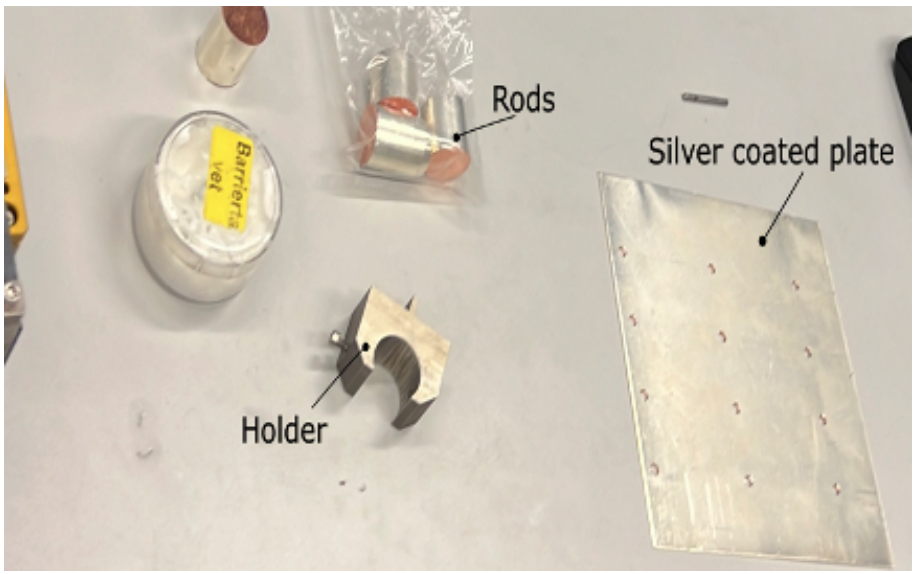


FIGURE 3.1: Test specimens for the friction test

Two main tests were conducted using the UMT, namely the friction test and the wear test. For consistency, silver coated specimens were used, although there were a few diferences in the sample preparation. The plate, mentioned in section 3.1, was used for all the UMT experiments. In the friction test, the plate was 150 mm in length and 150 in width. Linear holes were drilled to mount the plate in the UMT stage and adjust the tracking path easily in the friction test. Figure 3.1 shows the test specimens for the friction test. However, for the wear test, the plate was cut into smaller pieces, each 50mm in length and 30 mm in width. The mechanical properties such as the hardness and young modulus was measured for these specimen. By cutting the connecting rod into pieces of 20mm in length, the cylindrical samples were chosen. During the roughness measurement, it was observed that grooves were present in the sections of the connecting rod, probably a result of the turning during manufacturing process. These grooves can potentially affect tribological behavior, so it was important to take them into account.

### 3.1.3 Lubrication in switchgear contacts

The literature highlights the importance of dielectric lubrication for electrical contacts. Eaton uses Klüber's BARRIERTA grease [38], a perfluoropolyether (PFPE) synthetic oil for the electrical contacts within the SVS. This particular lubricant is known for its wide operating temperature range, ranging from -40°C to 260°C, which is beneficial for the performance of the SVS. Table 3.2 lists the properties of the lubricant.

TABLE 3.2: Properties of the BARRIERTA L55/2

| Property | Value |
|---|---|
| Minimum Service Temperature | $-40\,^{\circ}\mathrm{C}$ |
| Maximum Service Temperature | $260\,^{\circ}\mathrm{C}$ |
| Kinematic viscosity at $40\,^{\circ}\mathrm{C}$ | $420\,\mathrm{mm}^2/\mathrm{s}$ |
| Kinematic viscosity at $100\,^{\circ}\mathrm{C}$ | $40\,\mathrm{mm}^2/\mathrm{s}$ |
| Base viscosity | $8000\,\mathrm{mPa}s$ |

The exponential relation between temperature and viscosity of the lubricant is shown and plotted in figure 3.2 using [39].

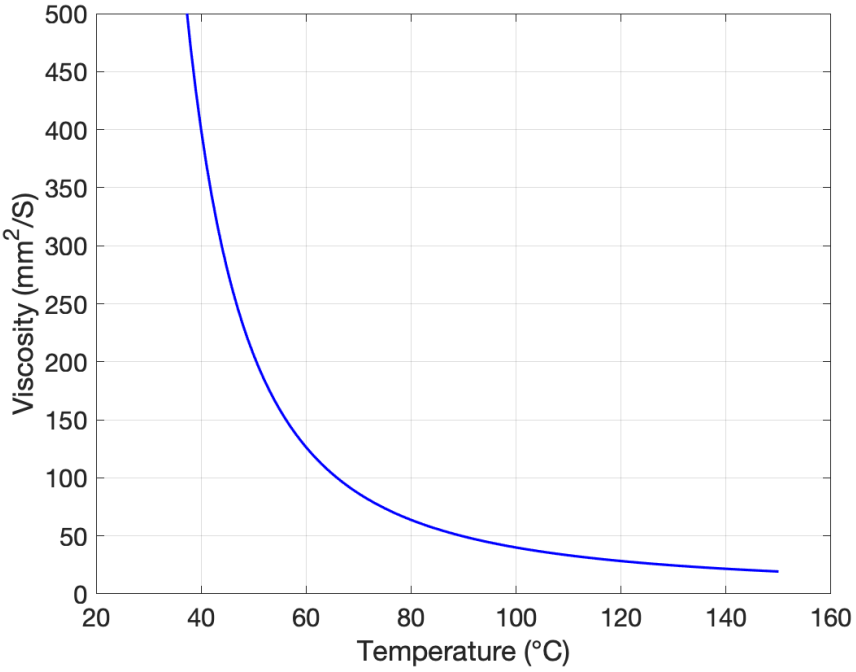


FIGURE 3.2: The viscocity vs temperature plot of the Barrierta grease

It is also essential to know what kind of lubrication regime the system involves. Therefore, to calculate the $\lambda$ ratio, equation (1.4) must be used. Consequently, it is necessary to determine the minimum film thickness ($h_{\min}$) of the lubricant for line contact. The minimum lubricant gap ($H_{\min}$) can be computed using the Dowson-Higginson method for EHL in line contacts, as as shown in Equation (3.1) [40]:

$$H_{\min} \approx 2.65 G^{0.54} u^{0.7} W_{2D}^{-0.13} \tag{3.1}$$

The material parameter ($G$), velocity parameter ($U$) and load parameter ($W_{2D}$) is listed in table 3.3 and expressed in equation (5.3):

$$G = \alpha_p E', \quad U = \frac{\eta_0 U_m}{E' R_x}, \quad W_{2D} = \frac{F}{L E' R_x} \tag{3.2}$$

The parameters were substituted first in equation (3.2) and then in equation (3.1) to calculate $H_{\min}$, which must be calculated with $R'$ to obtain the desired $h_{\min}$. The calculation determined that the minimum film thickness, $h_{\min}$, was 0.0233 $\mu$m. This thickness is then

| Parameter | Symbol | Value |
|---|---|---|
| Normal Load | $F$ | 8.1 N |
| Contact length | $L$ | 0.02 m |
| Reduced Young's modulus | $E^*$ | $126 \times 10^9$ Pa |
| Effective radius | $R'$ | 0.011 m |
| Effective velocity | $U_m$ | 0.005 m/s |
| Base viscosity | $\eta_0$ | 8 Pa·s |
| Pressure-viscosity coefficient | $\alpha$ | $\frac{L}{20}$ |

TABLE 3.3: Parameters used for the Dowson-Higginson line contact equation

divided by the surface roughness parameters, Rq, of both the connecting rod and the silver-coated plate. As described in section 3.2.2, the initial Rq value for the connecting rod is 0.68 $\mu$m, and for the silver-coated plate, it is 0.40 $\mu$m. Substituting these values into equation (1.3), a $\lambda$ ratio of 0.03 is obtained for initial contact conditions before wear test. This result indicates that the system operates under boundary lubrication conditions as discussed in the referenced literature [33].

## 3.2 Characterisation of the surface of test specimens

### 3.2.1 Coating thickness

Since the connecting rod and the tulip consist of the same substrate and coating material, one of the components was characterized. The reason for choosing the connecting rod is that in the tribological tests, mentioned in section 3.5, the connecting rod was used as the cylinder. The measurement of coating thickness has four steps: sectioning, embedding, grinding, and microscopy.

1. Sectioning: the connecting rod was cut into 10 pieces in the radial direction of the flat surface using an abrasive wheel. In the cross section of the connecting rod, the copper substrate was visible to the naked eye. However, the silver coating was only visible using a microscope.

2. Embedding: the abrasive wheel affected the surface of the specimens, so it was necessary to grind them. To mirror polish the cross-section of the cylinder to be able to see it under microscope they were embedded in epoxy resin and were mounted in a polishing holder. This holder can clamp three specimens and made the handling easier, it also serves to protect the edges of the specimens.

3. Grinding and polishing: Struers Tegramin-30 machine was used for this step. Wet silicon carbide grinding paper was used, with a grain size of 500, 1000, 2000 and 4000, for plane and fine grinding. The DiaDuo-2 with 9$\mu$m was used for the polishing for 4 minutes.

4. Microscope: the scanning electron microscope (SEM), explained in section 3.2.3., was used for measuring the coating thickness.

The cross section of a connecting rod under SEM is shown in figure 3.3. This measurement confirmed that the average thickness of the silver coating is 10 $\mu$m.

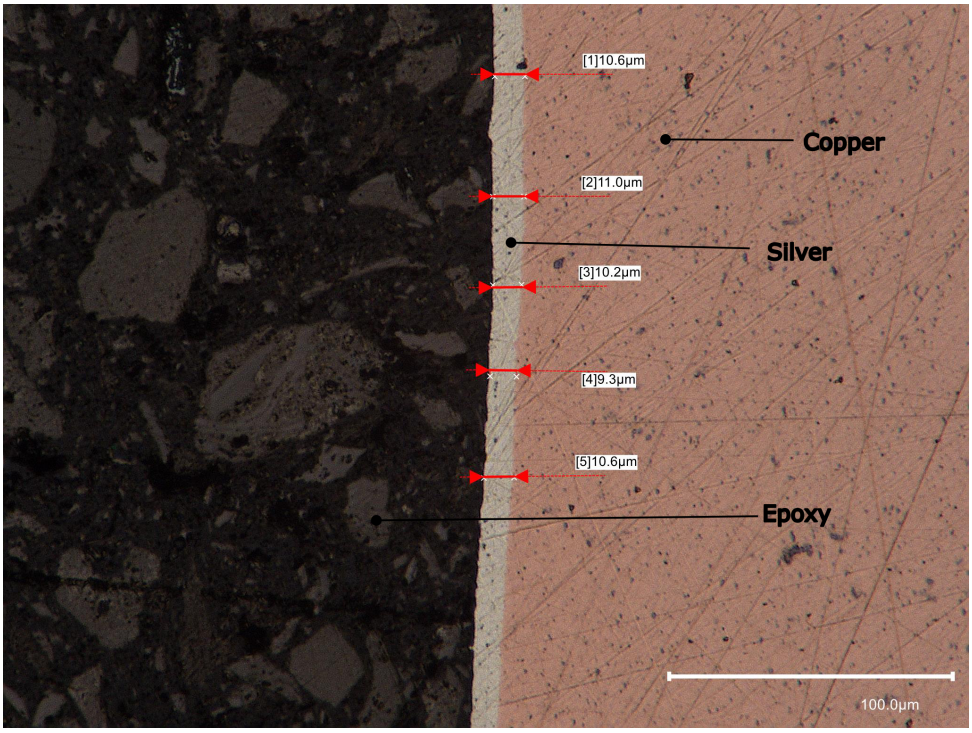


FIGURE 3.3: Coating thickness measurement of connecting rod

### 3.2.2 Surface profile and roughness

Confocal microscopy was used to measure the roughness of the specimens. This method can help to measure the change in the roughness before and after the wear test. In addition, it measures the change in coating thickness by measuring the change in curvature of the cylindrical specimen before and after the tests. The roughness parameters according to ISO 21920-2:2021, were measured using the confocal microscope and listed below:

- Ra (Average Roughness): The arithmetic mean roughness is the primary parameter used in surface profile analysis. It represents the mean value of the heights of peaks and depths of valleys in a specified area.
- Rq (Root Mean Square Roughness): The root mean square roughness is calculated as the square root of the average of the squared heights of peaks and valleys within a specified area.
- $\delta$z (Height change): The measured height of the contact area reflects any changes in coating thickness.

Figure 3.4 shows a confocal image of the surface of the connecting rod before the tribological wear test. It can be observed that there is a texture on the surface and Ra = 0.45 $\mu$m and Rq = 0.52 $\mu$ m was measured. The values will be compared with the values obtained from the samples after the wear test, mentioned in section 4.3. The grooves in the coating on the connecting rod serves two functions: to trap wear debris and to function as lubricant reservoirs. The presence of these grooves, however, could also contribute to inconsistent wear patterns, influenced by factors such as lubricant distribution, viscosity, and potential degradation under certain environmental conditions.

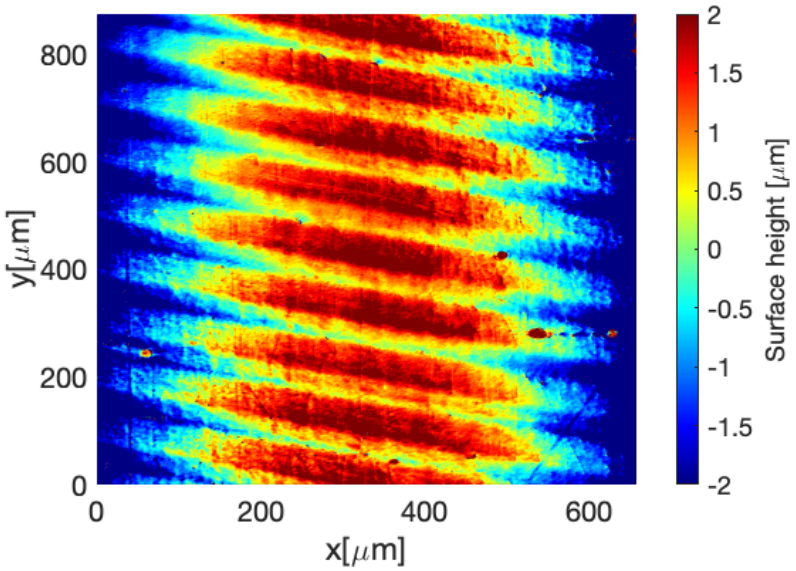


FIGURE 3.4: 3D imaging of the connecting rod

### 3.2.3 Surface stiffness and hardness

Nano-indentation is a technique used to evaluate the mechanical characteristics of materials, including their elastic modulus and the hardness of the surface, on the nanometer scale. This method involves the loading of a diamond indenter onto the material's surface under precisely controlled force and penetration depths. It generates a load-displacement curve, which charts the applied force versus the depth of indentation [41].

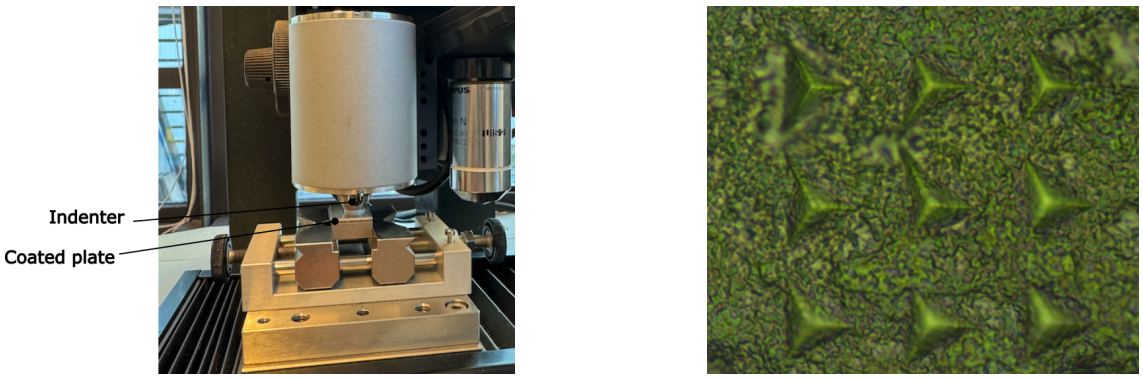


(A) Test setup

(B) three-sided pyramid marks on the surface

FIGURE 3.5: Nano-indentation on the silver coated plate

The mechanical properties of the silver coated plate, mentioned in sections 3.1.1 and 3.1.2, were measured using nano-indentation, as shown in figure 3.5a. The plate was cut into three samples of 10mm in length and 10mm in width. A Berkovich indenter (three-sided pyramid) was used for this indentation test under load. The three samples were indented at 9 different spots per sample. The reason for measuring it on different spots is to validate the properties and take the mean value. Figure 3.5b shows the indentation marks on the surface of a sample.The Oliver and Pharr (O&P) method [42] was used to analyze the unloading segment of the load-displacement curve, essential for calculating the elastic

modulus and hardness of the material. Using the stiffness and the indenter area function, the hardness and the elastic modulus are precisely calculated, providing key information on the mechanical behavior of the material under load.

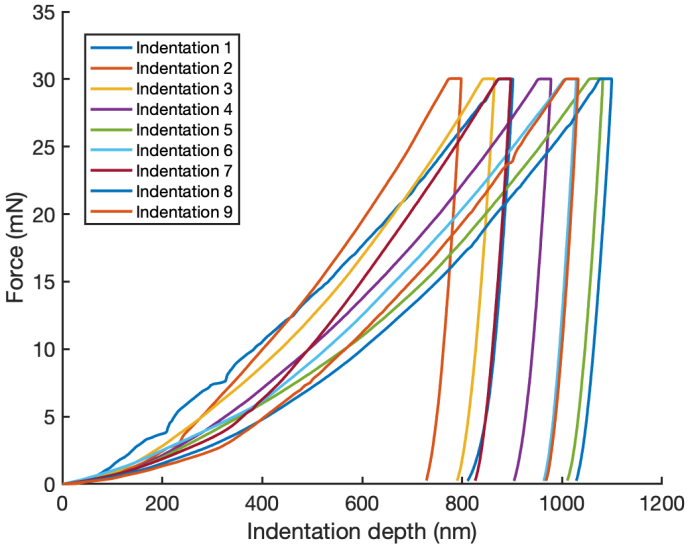


FIGURE 3.6: Nano indentation curves for sample 2 at 30 mN

Indentation depth is a crucial consideration in coated systems because if the indenter penetrates too deeply, it measure a combination of substrate and coating properties, while at a low enough loads only the coating properties are measured. A common approach for just measuring the properties of the coating and not taken the substrate into account, is to restricting the measurement to a maximum indentation depth of no more than 10% of the coating thickness [43]. Furthermore, the indentation must also accommodate the surface asperities, necessitating a depth that exceeds the surface roughness Rq value of 430 nm as measured using the method in section 3.2.2. Consequently, the appropriate indentation depth is set between 430 nm and 1000 nm. Figure 3.6 shows the load-indentation depth curve for sample 2. It is evident from the curve that measurements are confined to the coating, as the indentation depth remains below 10% of the coating's thickness and exceeds the surface roughness Rq value. This means that the measurements results in properties of only the silver coating.

Table 3.4 lists the hardness and the young modulus of the smaples obtained from the nano indentation. The average of Young's modulus from the three samples are 115 GPa and the average hardness is 1.333 GPa.

TABLE 3.4: Hardness (HIT) and Youngs modulus(EIT) as obtained from Nano-indentation tests

| **Property** | **Sample 1** | **Sample 2** | **Sample 3** |
|---|---|---|---|
| **HIT (O&P) Mean [GPa]** | 1.246 | 1.481 | 1.273 |
| **Std Dev** | 0.269 | 0.272 | 0.186 |
| **EIT (O&P) Mean [GPa]** | 117.497 | 119.313 | 112.868 |
| **Std Dev** | 14.115 | 10.194 | 13.667 |

### 3.2.4 Surface morphology and elemental composition

The SEM is used to observe and analyse the surface morphology of samples at high resolution. This microscope operates by scanning the sample surface using a focused beam of electrons, which generates various signals as it interacts with the sample surface. Instrument detectors are capable of capturing secondary electrons and backscattered electrons, as well as X-rays emitted from the sample. These detections result in detailed analysis of the samples surface texture and composition [44].

Another advantage of this method is that SEM can be used with energy-dispersive X-ray (EDX). This detector is used for elemental analysis or chemical characterization of the sample. The spectrum obtained from the EDX consists of peaks corresponding to the characteristic X-ray lines of the elements that can be found on the surface of the sample. This allows for the determination of the elemental composition by measuring the concentration levels of the elements located on the samples surface [45].

The SEM-EDX technique is used to analyze the samples after the wear test, mentioned in section 3.5.2. Following the wear tests, the connecting rod was observed under SEM to look for the chemical composition of the surface and to analyze the possible wear mechanisms.

## 3.3 Pressure measurement foil

In section 2.3.2, the following assumption was made: the contact between the the circular spring and the tulip section is considered as a cylinder on a plane configuration. A 16.9 MPa contact pressure was measured and will be measured using Fujifilm sheets [46].

FIGURE 3.7: The interaction between two cylinder using the sheet [46]

These sheets can be placed between the contacting surfaces and contain tiny capsules. When pressure is applied, these capsules break open and release a substance that generates a red color on the sheet. The colorized sheet is then scanned and by the use of Matlab code, the pressure distribution is determined based on the color density. Figure 3.7 shows an example of two contacting cylinders, where a red line contact can be observed.


FIGURE 3.8: The mono-sheet placed at the springs position

To validate the pressure distribution between the circular spring and the tulip section, a mono sheet for pressures between 10-20 MPa was utilized. Figure 3.8 shows the placement of the mono sheet at the contacting surfaces. The contact pressure obtained from Matlab was 15.2 MPa, which is within a margin of 10% of the calculated 16.9 MPa. These results shows that model describes accurately the experimental situation in the same configuration.

## 3.4 Performance test

The performance tests are experiments which will help to measure the friction force occurring during the interaction of the connector mechanism components. The goal of this test is to simulate the connector mechanism making multiple contact events, without temperature effects. The results of penetration force vs distance from the performance test will be used to validate the results from the ABAQUS model described in section 2.1. Figures 3.13b and 3.13a show the setup of the performance test. The vertical separation distance between the two components was 1mm and was considered the starting point. The tulip slides 20mm around the connecting rods surface with a reciprocating motion. This was repeated three times and in the force against travel plotted. The load cell was able to measure up to 5kN. The arrow shown in 3.13a shows the movement of the tulip.

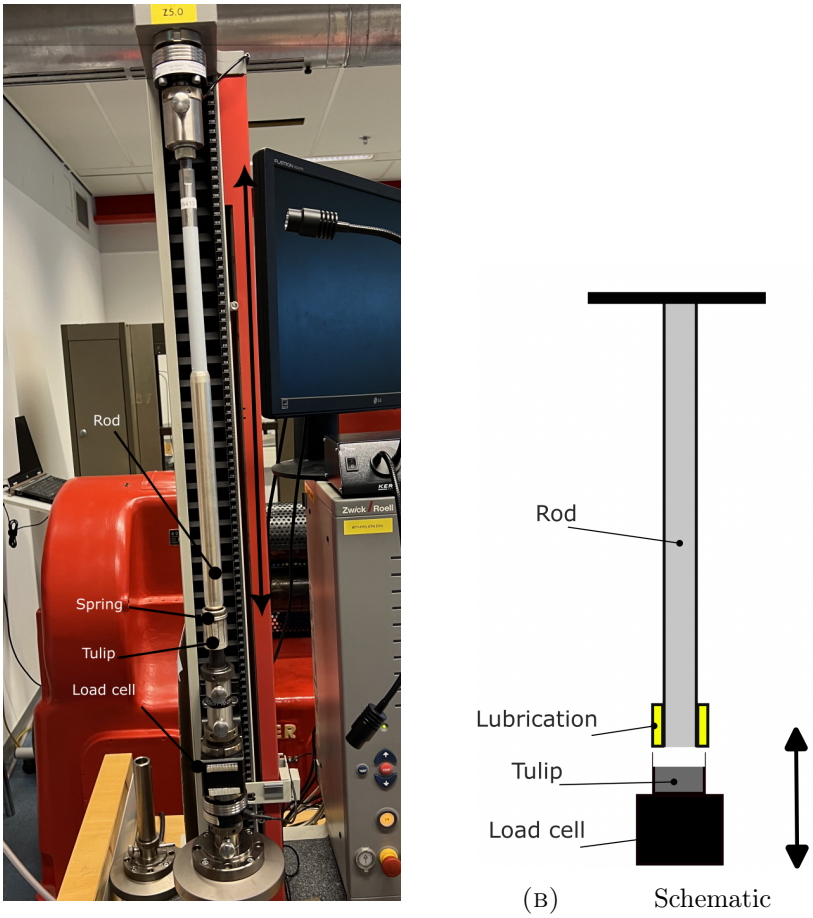


(A) Experimental setup (B) Schematic overview

FIGURE 3.9: The representation of the performance test

Two different samples were used for the performance test. The important parameters during this test are: velocity and sliding distance. Since the connector mechanism is manually driven, the loading velocity could be any value, varying from really fast to slow conditions. The following assumption was made:

- fast condition: 10 mm/s
- normal condition: 5 mm/s
- slow condition: 1 mm/s

Since the sliding distance is 20 mm, these velocities will make the (dis)connecting time 2, 4 and 20 seconds. According to Eaton, the fast and normal condition of these realistic values for the use of the connector mechanism. It is done to check if the velocity has an impact on the force. The results are plotted and can be found in figure .3 in Appendix B.

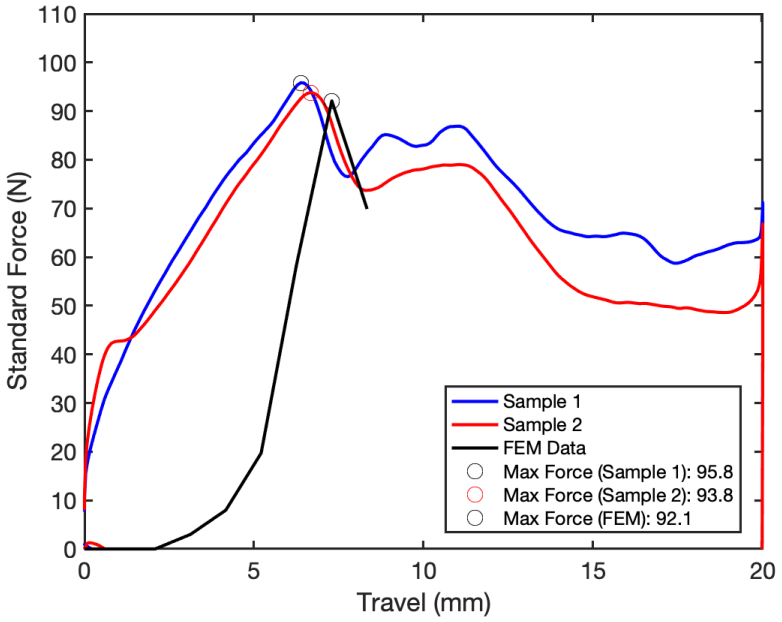


FIGURE 3.10: Comparison and validation of the performance test en FEM at 10 mm/s

Figure 3.10 shows the results of the fast condition under different samples. It can be observed that both samples reach around 6mm around the 95N. However, the FEM results, under the same condition, was plot together. The FEM model calculates 92.1N, which is close to the results of the performance test. The two bumps, after the peaks, are not observed in the FEM model. This might be that the shell is not touching point 'A' in figure 2.2a. It makes only contact in the red line of figure 2.2. This plot shows that the FEM can be validated using the performance test.

## 3.5 Universal mechanical tester

Bruker's UMT is a tribometer that can be used to measure friction and wear of different contact configurations. The UMT can mimic contact conditions like the connector mechanism under different operating conditions, such as temperature, load, and velocity. It consists of a modular drive, which can be used for reciprocating, linear, and rotary mo-

tions, as shown in figure 3.11a. Besides these drives it can be combined with environmental testing by placing the drives inside a temperature or humidity chamber. For loading, the DFH-50 load cell with a working range up to 50N, was used.

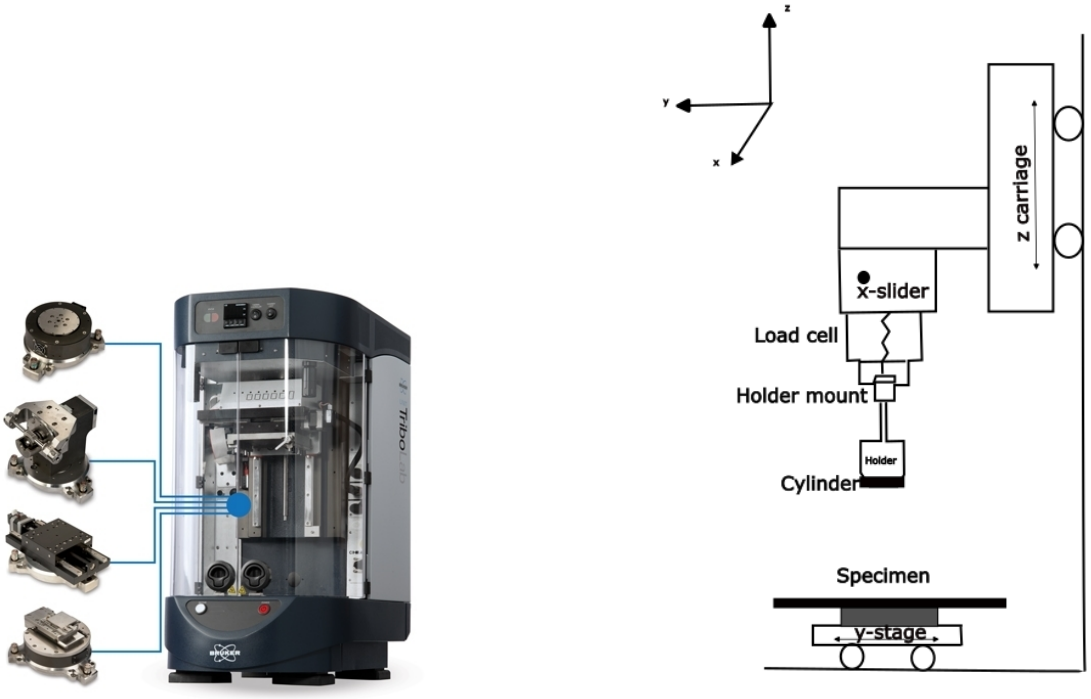


(A) Bruker's UMT [47]

(B) Schematic of the friction test using UMT

FIGURE 3.11: The UMT that has been used for both the friction and wear tests

Figure 3.13a shows how the UMT has been adjusted to measure friction in the cylinder on plane contact. This setup was also used for the wear test, only the y-stage is different. The UMT consists of three stages which can move in the x, y and z direction. The specimen was mounted on a linear drive, which can just move in the y-direction. The connecting rod is mounted on the x-slider, which moves the connecting rod through the x-axis. However, the height of the connecting rod was adjusted by z-carriage. The connecting rod is able to move in both x-direction and z-direction, since the x-slider was mounted on the z-carriage. A stepper motor drive was used to translate rotational into linear motion for the movement of the x-slider, y-stage and the z-carriage. The load cell is directly connected to the holder and a suspension block. The plates of the suspension blocks act as a spring. This means that during contact between the rod and the plate, possible shock loads can be reduced.

### 3.5.1 Friction results

The first test using the UMT was the friction test. The goal of this was to measure the COF of the lubricated contact of the cylinder in the plane configuration. The velocities similar to that in the performance test were used for this test. However, this time the load was set manually. To check if the COF changes with load, the following loads were chosen randomly: 2N, 5N, 10N, 18N, 25N and 45N.

Figure 3.12 shows the configuration of the friction test. The plate was mounted on a linear drive. This linear drive was able to move in the y direction to adjust the position of the track. On one side of the plate, 24 tracks can be used. The reason for repeating this test three times is to validate every test with different parameters.

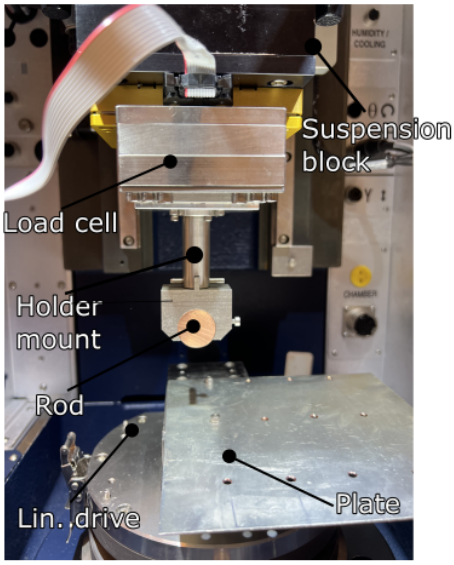


FIGURE 3.12: The friction test configuration

The COF was derived by dividing the friction force by the normal force during steady-state conditions in figure 3.13a. Each friction measurement consisted of three separate measurement, from which the average COF was calculated. Error bars represent the standard deviation of these averages. The initial and tail-end friction data were excluded to filter out anomalies in the COF values.

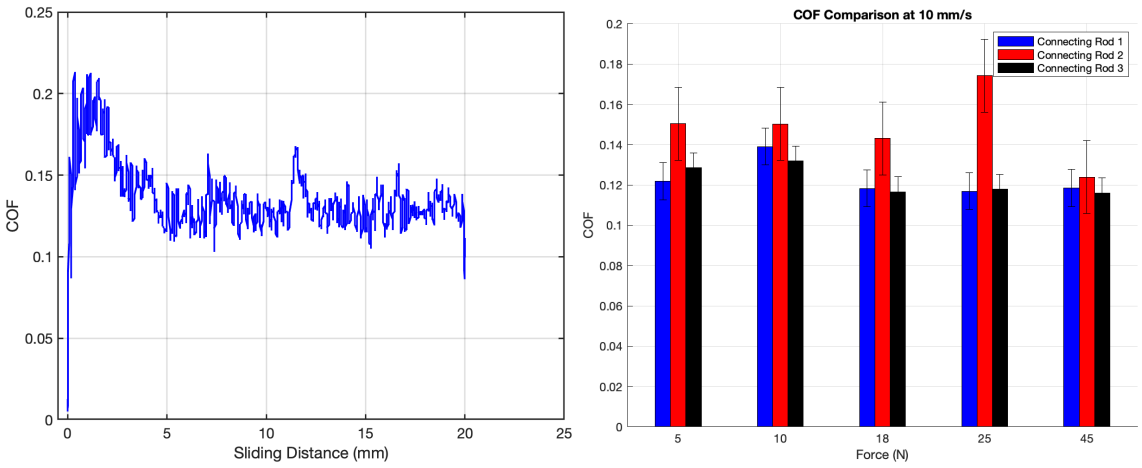


(A) Signal of a friction plot at 18N

(B) COF comparison at 10 mm/s

FIGURE 3.13: Friction and coefficient plot at differences forces

The results in 3.13 showed the COF values for connecting rod 1 and connecting rod 3

are approximately 0.12, the values for connecting rod 2 show a deviation from this trend. This variation can be explained by the fact that this was the final test performed and the rear side of the plate used was utilized. Bending and other forms of physical alteration from previous tests could have influenced the surface interaction, leading to the observed discrepancies in COF values. The other results with different velocities can be found in figure .4 in Appendix C.

### 3.5.2 Wear test

The wear test is performed to study the degradation and wear mechanisms in the connector mechanism and help predict the lifetime. This test is almost identical to the friction test, explained in subsection 3.5.1, but there are some differences. The main difference is that in the wear test temperature was varied using the heating chamber, with a temperature range of 400°C. With these adjustments the wear test has the following parameters: velocity, force, temperature and stroke. Figure 3.14 shows the wear test setup with an oven.

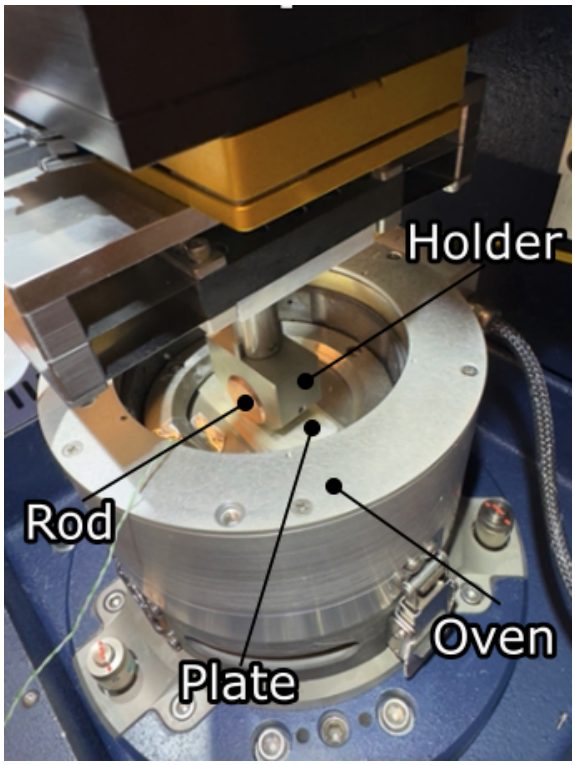


FIGURE 3.14: Wear test: cylinder on plane configuration

On the three velocities used in the friction test only one velocity of 10 mm/s was chosen for the wear test. The connector mechanism is driven by professionals, for the push-in and push-out, and they expected to perform the operation in shortest time. The calculated $F_L$ of 8.1N, mentioned in section 2.3.4 is used for this test, since the connecting rod and tulip contact have the same resulting contact pressure.

It is important to do the test in normal and extreme thermal conditions. According to the NEN-EN-IEC 62271-1 standard, the maximum temperature can be 115 °C. The second parameter is just the temperature rise: 75°C. The average ambient temperature of the Netherlands was also used: 20 °C. The final temperature value was 50 °C, which is the

maximum ambient temperature in arid tropical conditions.

The final parameter is the stroke number. One stroke in this test is: push-in and push-out. The recommended lifespan of the SVS is 1000 strokes. Since the use of the SVS is customer dependent, it can be used daily, weekly, and monthly in a year. Therefore the parameters are: 12 strokes (monthly), 52 (weekly), 365 (daily), 1000 (lifespan). Table 3.5 lists the matrix for the wear test. It was not an option to choose every possible situation. Therefore there were three choices made:

- 365 strokes was chosen to test it with every possible temperature. The reason is that this value is almost 1/3 of the SVS lifespan. This can give a good indication of the wear.
- 75°C was chosen for all possible stroke number. The reason for choosing this temperature is that not everywhere where the SVS is in use has an ambient temperature of 40°C as explained in the standard. Therefore just the maximum temperature rise, 0 °C ambient temperature, is something what can be considered as average.
- Extreme conditions: it is also interesting to see what the effects will be in extreme conditions. Therefore the maximum lifespan of 1000 strokes in maximum temperature conditions was chosen and a test of 3650 strokes (everyday for 10 years) in 75°C was added to the test.

TABLE 3.5: Test matrix for wear test

| **Test Nr** | **Stroke** | **Temperature (°C)** |
|---|---|---|
| 1 | 365 | 20 |
| 2 | 365 | 50 |
| 3 | 365 | 115 |
| 4 | 365 | 75 |
| 5 | 12 | 75 |
| 6 | 52 | 75 |
| 7 | 1000 | 75 |
| 8 | 1000 | 115 |
| 9 | 3650 | 115 |

# 4 Experimental results

These evaluations were critical in assessing the wear resistance and longevity of the coating under test conditions, providing information on the effectiveness of the coating in protecting the connecting rod during use in switchgear.

## 4.1 Connecting rod

Following the wear tests, the connecting rod underwent detailed examination using confocal microscopy, as mentioned in section 3.2.2 of the thesis. This examination focused on two primary parameters of the test specimens:

1. The specimens surface roughness of the contact region surrounding the wear track on the connecting rod, measured before and after the wear tests. The objective was to understand how the sliding wear in the connecting rod and plate contact affected the surface roughness and texture.
2. The increase of the coating thickness on the connecting rod due to material accumulation or decreased as a result of material removal and adhesion to the counterbody.

### 4.1.1 Surface roughness of wear track

The expectation for a uniform wear track of 20 mm across the surface of the connecting rod following the wear test was not met. Instead, wear tracks were identified in patches on the left, middle, and right sections of the surface. Such variability in wear tracks can stem from multiple factors, including misalignment of contact. Among the causes are the curvature of the counterbody due to bending while mounting on the fixture and the edge effects on the connecting rod, which influence load distribution adversely. Figure 4.1 shows

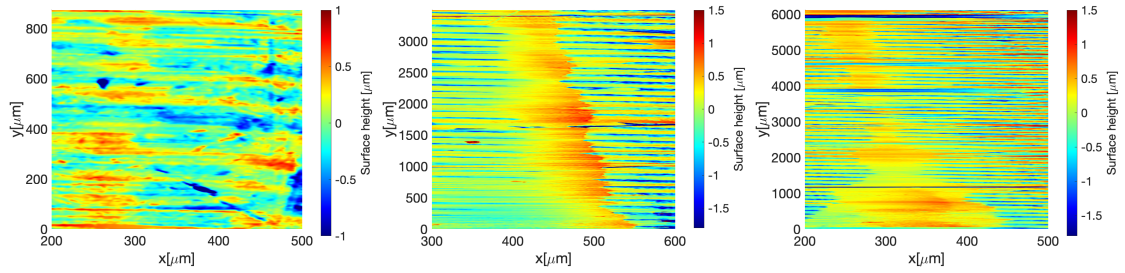


(A) Stroke number: 52 (B) Stroke number: 365 (C) Stroke number: 1000

FIGURE 4.1: Wear track on the connecting rod at 75 °C as a function of number of strokes

the possible wear tracks that was found on the surface of the connecting rod. Figure 4.1a

height differences in the wear track. Figure 4.1b shows a uniform wear track, and figure 4.1c shows material addition on the track. A notable solution to minimize these misalignments involved removing the edge effects of the connecting rod with chamfers. Furthermore, variations in surface roughness between contact interfaces contributed to the inconsistency in the wear tracks.

### 4.1.2 Surface roughness measurement

In the study of surface roughness on a connecting rod, measurements of Ra and Rq values were crucial for defining the surface texture after the wear tests. Each connecting rod sample was examined by surface height measurements taken from three parts of the contact length: left, middle, and right. Due to the observation of inconsistent wear tracks across the samples, as explained in section 4.1.1, certain specific areas were selectively measured to ensure accuracy.

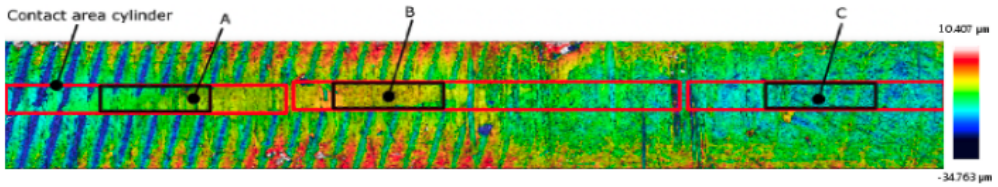


FIGURE 4.2: Wear track 365 number of strokes and 50 °C

For each sample, nine distinct measurement regions were chosen by dividing the measured section (left, middle, right) into three sections. This comprehensive approach is shown in figure 4.2, which includes three regions marked in red and black. The red diagrams, representing the contact area determined in section 2.4.4, are defined by the contact width of 45 $\mu$m and a length of 20 mm. These red regions were strategically placed at the center of the wear tracks, acknowledging that in higher number of strokes, the actual width of the wear track exceeded the expected contact width according to Hertz. The reason is that plasticity and increased surface roughness will make the track apparently wider. Within each red region, three smaller areas labeled A, B, and C were identified for detailed roughness measurement. The dimensions for these specific areas remained constant in width at 45 $\mu$m, but the length was reduced to 1000 $\mu$m. This decision was based on the goal of measuring the contact across 10 grooves, providing a more localized and precise assessment of the surface roughness through the Ra and Rq values within these areas.

Before performing the wear test, baseline surface roughness measurements were obtained, as mentioned in section 3.2.2, with mean values determined as Ra = 0.45 µm and Rq = 0.52 µm. If the wear test measurements exceed these baseline values, it indicates an increase in surface roughness, suggesting that sliding wear has roughened the surface texture. However, measurements significantly below these baselines imply that the surface has become smoother, indicating a flattening effect as a result of the sliding wear.

Following the analysis, for each test number, a total of 18 different values of Ra and Rq were obtained, measuring the variations in surface roughness in various contact regions and can be found in table .1 and table .2 in Appendix D. These measurements provide detailed information on the surface condition in the contact region of the connecting rod

after the wear test. The mean values of the Ra and Rq measurements were plotted against the stroke number and temperature to understand the overall impact of the wear test on the surface roughness of the connecting rod samples.

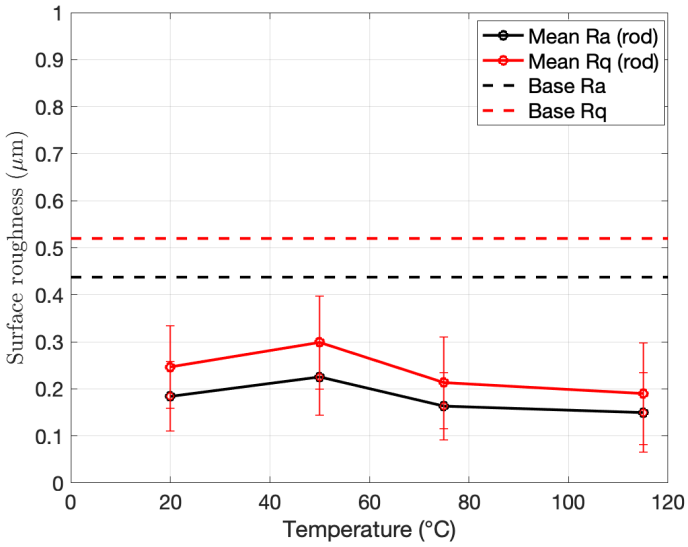


FIGURE 4.3: The roughness change of the connecting rod at 365 strokes against all possible temperature

Figure 4.3 shows the roughness change of the connecting rod at 365 strokes against every possible temperature. It can be observed that the significant decrease in both Ra and Rq values, with reductions surpassing 50% compared to the base values of Ra and Rq. This shows that the number of operational strokes and changes in temperature has a strong impact on reducing surface roughness. Despite a general trend towards lower roughness values, there were notable differences at certain temperatures: the roughness peaked at 50°C showing the highest levels, while the lowest roughness was recorded at 115°C This pattern shows the effect that temperature, along with stroke number, has on the wear process and its influence on the final texture of the surface.

The second analysis focused on plotting change in roughness against all strokes at a fixed temperature of 75°C, as shown in figure 4.4. This plot revealed that at lower stroke counts, specifically 12 and 52 strokes, the Ra and Rq values remained close to those of the connecting rod's initial Ra and Rq value. This indicates that lubrication remained effective in these early stages of testing, preventing significant wear and changes in surface roughness. However, starting from 365 strokes, there was a significant drop in Ra and Rq values. Interestingly, the roughness measurements for 365, 1000, and even 3650 strokes were found to be closely aligned. This pattern suggests that the reduction in surface roughness was constant after reaching a certain level of wear, evidenced by the decrease in Ra and Rq values up to 365 strokes, followed by a slight increase or stabilization at the 1000 and 3650 strokes. These findings indicate that after a critical number of strokes, further increases in stroke numbers do not significantly alter the roughness, hinting at a steady state condition where the surface undergoes minimal changes.

A final analysis was to determine the effect of extreme temperatures on surface roughness.

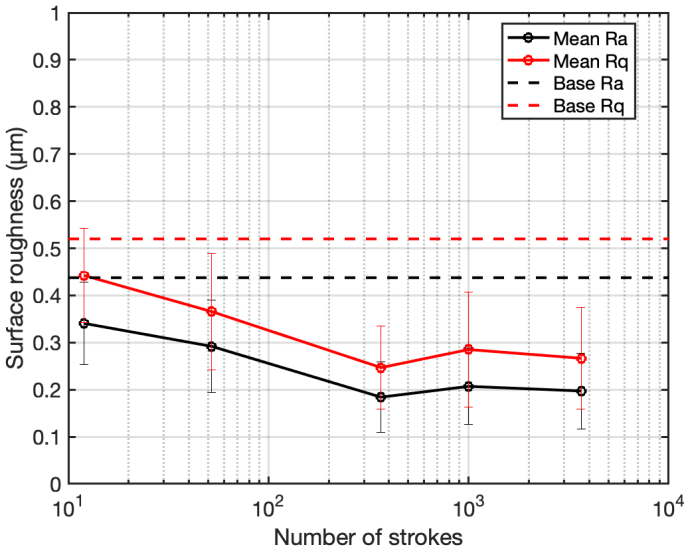


FIGURE 4.4: Roughness measurement at all strokes against 75°C

The roughness values at stroke numbers 365 and 1000 against temperatures of 75°C and 115°C were plotted and is presented in figure 4.5. This comparison focused on evaluating the significant influence of temperature on wear-induced changes in roughness.

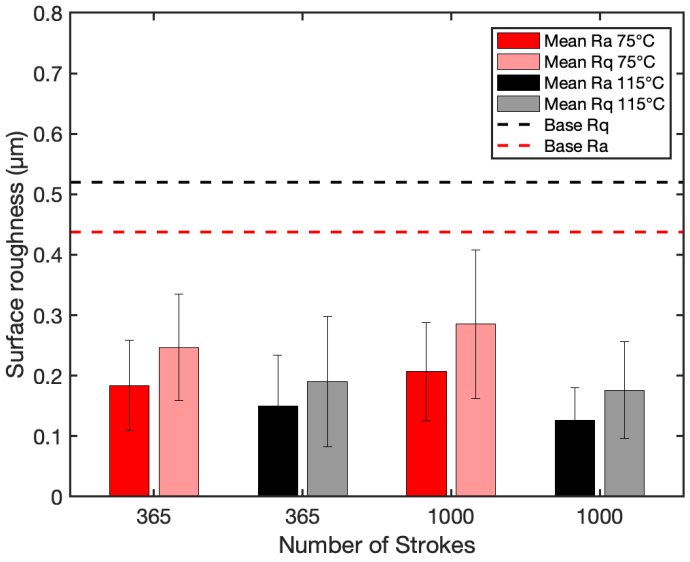


FIGURE 4.5: The roughness of the connecting rod at 365 and 1000 strokes against 75°C and 115°C

The SVS most extreme condition, 1000 strokes at 115°C resulted in the lowest Ra and Rq values observed. This indicates that the combination of high stroke number and temperature significantly enhances the wear process, leading to a smoother surface. When comparing the effects of 1000 strokes at 75°C and at 115°C, the difference made by the higher temperature is pronounced, suggesting that higher temperatures have a substantial impact on the wear mechanism and surface roughness. A similar trend was observed for the test at 365 strokes at 75 °C and 115°C. However, even the results shows the same pat-

tern for higher temperatures, the measured roughness values does not show a significant difference. This concludes that the temperature has not a big impact on the roughness change of the surfaces.

The results obtained from surface roughness measurements on the connecting rod indicate that with increasing stroke numbers and higher temperatures, the lubrication film tends to degrade. This degradation leads to smoother and flatter surfaces due to reduced lubricant effectiveness, which, while potentially decreasing electrical contact resistance by removing junctions, primarily results in increased metal-to-metal contact. Consequently, this direct contact and interfacial shear between surfaces escalate adhesive wear. Thus, despite the initial appearance of a smoother surface, the overall impact is detrimental due to the increased wear from insufficient lubrication.

### 4.1.3 Coating thickness

At the contacting region of the connecting rod, an increase of surface height was observed, which occurred in all stroke numbers. Furthermore, grooves effectively "vanished" due to the infill of wear debris during sliding. This resulted in an increase in coating thickness at specific regions of the wear tracks. Figure 4.6a shows the surface region of the connecting rod at 12 strokes, which consists of both the grooves and the filling/flatting of those grooves.

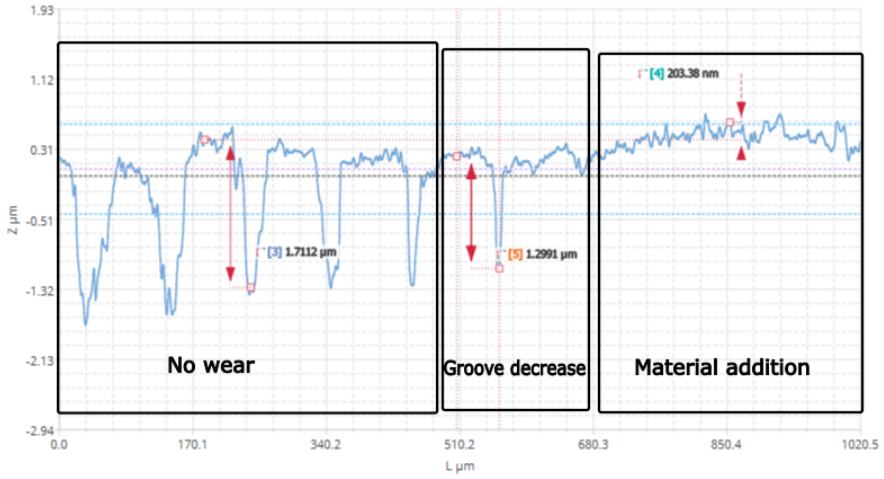


(A) Profile of the wear region

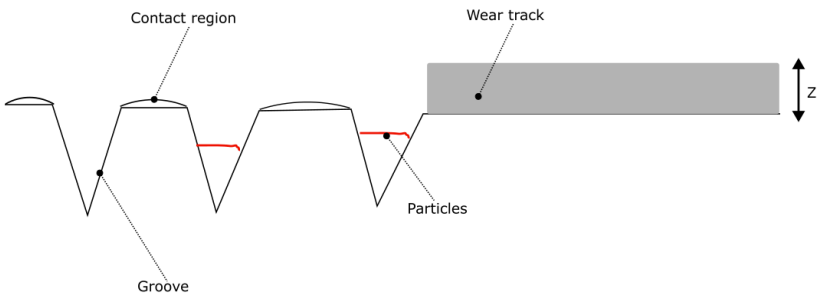


(B) Schematic overview of the coating increase process

FIGURE 4.6: Coating thickness change of the surface region on the connecting rod

In regions where wear tracks were not evident, the initial state of the connecting rod remained unchanged, indicating that the grooves did not change from their original condition. In these regions, the average depth of the groove was measured at 1.7 $\mu$m. However, close to the wear regions, it was observed that debris had accumulated inside the groove areas. This shows that the wear progressed to the extent of filling up the grooves, after which an increase in the layer's coating thickness was observed. This pattern was consistent across every evaluated number of strokes. Specifically, after 12 strokes, a new thickness of 0.2 micrometers was recorded. Figure 4.6b shows the schematic of the contact region of the connecting rod.

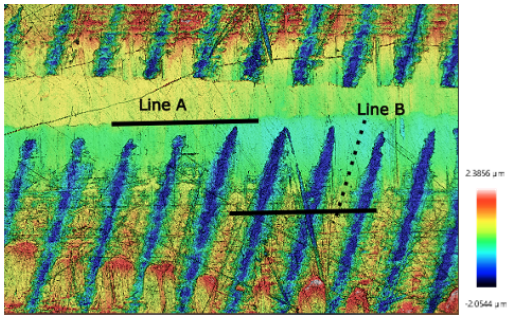


FIGURE 4.7: Approach for the coating increase measurement

The methodology for measuring surface roughness, as described in section 4.1.2, was applied again, with some adjustments due to differences in the diameters of the samples and is shown in figure 4.7. To account for variability and inconsistency of the wear tracks, the following approach was used: measuring the height of non-contacting areas (line B) and comparing those values to the heights measured within the wear tracks (line A). In this method, three sections on the cylinder were chosen for detailed observation.

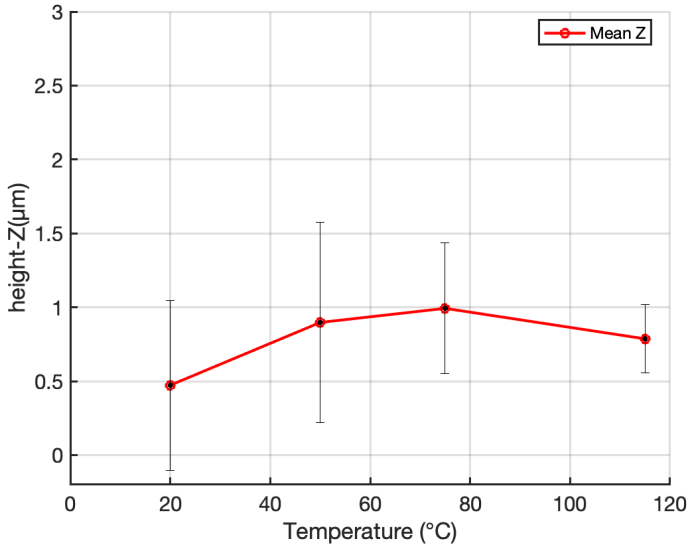


FIGURE 4.8: Coating thickness change at 365 number of strokes

Figure 4.8 shows the coating thickness increase at 365 number of strokes in relation to the temperature. The results indicate that for temperatures of 50°C, 75°C, and 115°C, there is a increase in coating thickness around 1 $\mu$m. As temperatures increase, the viscosity of the lubricant decreases. This reduction in viscosity leads to more frequent contact between asperities, thereby enhancing boundary shear stress. All this results in more adhesive wear.

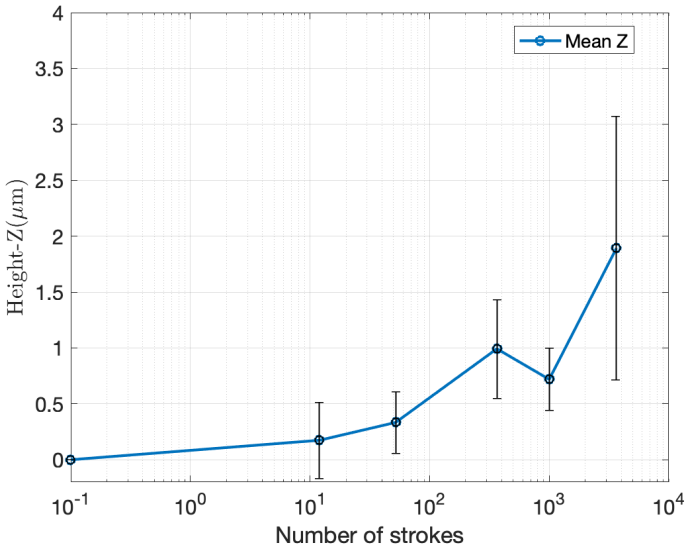


FIGURE 4.9: Coating thickness change at 75°C

Figure 4.9 shows the relationship between the number of strokes and the change in coating thickness at 75°C. For 12 and 52 strokes, a slight increase in thickness was observed ranging from 0.17 to 0.30 $\mu$m, indicating that at these counts, the grooves were completely filled. Conversely, at 365 and 1000 strokes, only a minimal change in thickness was observed. It was only at 3650 strokes that a significant thickness increase close to 2 $\mu$m was observed. The results shows that at a fixed temperature by increase of the number of strokes an increase of the coating thickness as expected based on Archard's wear law.

## 4.2 Silver coated copper plate

Another component in the wear test configuration involved a silver-coated copper plate. In alignment with the measurement procedures applied to the connecting rod, this component underwent examination after the wear test. A measurement of the roughness of the surface was performed. Additionally, instead of evaluating changes in the coating thickness, an elemental analysis was performed using SEM-EDX to analyze the deposited on the surface.

### 4.2.1 Surface roughness measurement

The method to measure surface roughness on the silver coated plate was different from the approach used for a connecting rod due to the three uniformly distributed scratches present on the plate. Consequently, rather than assessing the surface roughness of an region of the contact width of the connecting rod, the measurement focused on a profile located centrally among the three scratches, as shown in figure 4.10a .

This measurement was performed across all possible temperatures for the stroke number

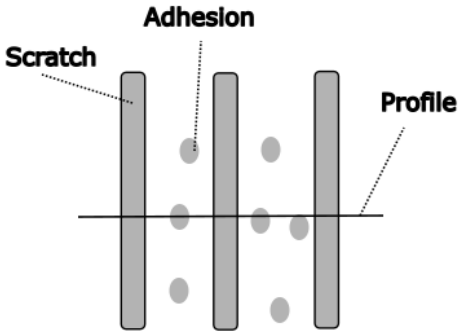


(A) Schematic overview of how to measure the wear track on the plate

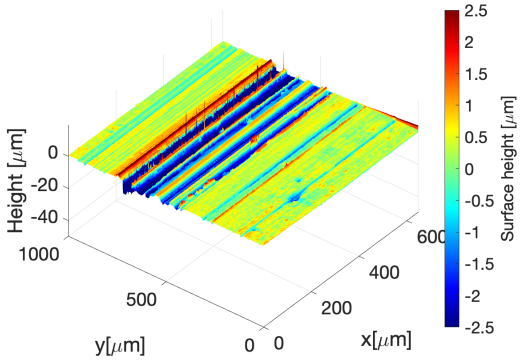


(B) 3D confocal image of one scratch

FIGURE 4.10: The measured profile on wear track for the plate at 365 strokes

of 365, aiming to achieve a supplementing pattern compared to that of the connecting rod. This approach was based on the hypothesis that adhesive material transfer would lead to an increase in the surface roughness of the plate beyond its original state, since the connecting rods surface roughness parameters Ra and Rq decreased by more than 50%. The baseline roughness of the plate was determined as Ra = 0.33 $\mu$m and Rq = 0.45 $\mu$m.
.

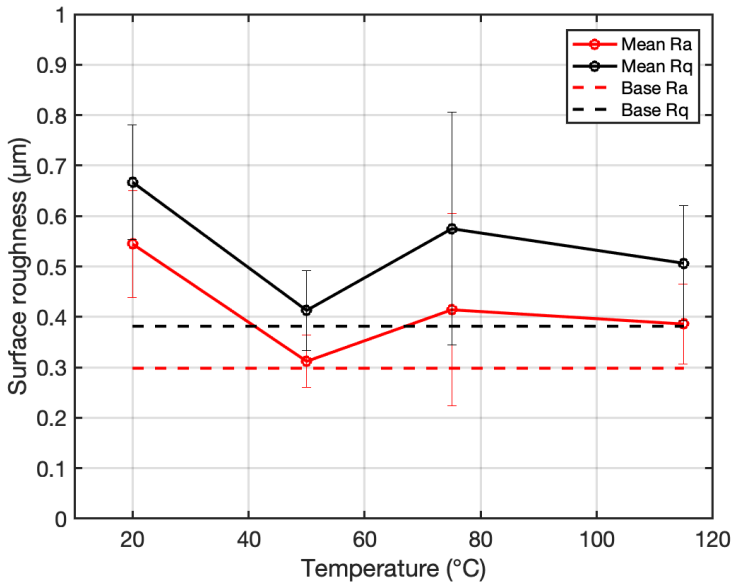


FIGURE 4.11: The measured Ra and Rq values for the plate at 365 strokes under several temperatures

The findings from the roughness measurements of the plate are presented in Figure 4.11 and can be found in table .3 in Appendix D. As expected, there was a significant rise, compared to the initial values of the plate, in both Ra and Rq values, indicating that the surface has become rougher due to adhesive material transfer to the counter-body.
The roughness surface change of the connecting rod and the silver coated plate are plotted

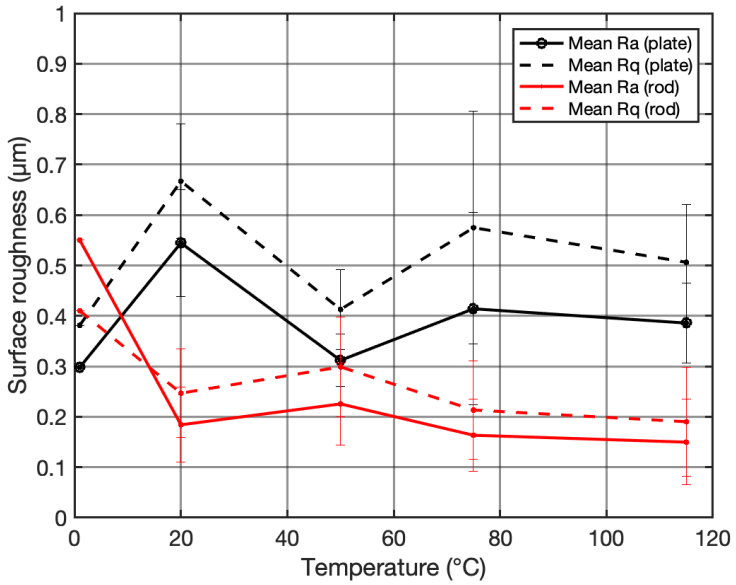


FIGURE 4.12: The measured Ra and Rq values for the plate and connecting rod against each other

together in figure 4.12. At X=0, the baseline Ra and Rq values of both the connecting rod and plote were plot. As expected, both surfaces are reflecting the same pattern. However, for 115 °C the plate roughness less compared to smoothing of the connecting rod. This was also observed in section 4.2.2 in figure 4.14.

### 4.2.2 Scanning electron microscope

Confocal measurements from the connecting rod indicated that adhesive wear had occurred, leading to an increase in the coating thickness. Elemental analysis using SEM-EDX, as mentioned in section 3.2.4, detects the presence of unwanted materials or traces of copper, which could indicate material transfer or contamination during the wear process. Additionally, the appearance of black marks on the surface of the sample tested at 3650 strokes at 75°C was a point of interest. Samples tested for 365 strokes at 75°C, 365 strokes at 115°C, and 3650 strokes at 75°C, were chosen for the analysis. The reasons for choosing these samples are as follows:

- Temperature influence: When comparing samples subjected to temperatures of 75°C and 115°C, both at 365 strokes, the effect on temperature on surface characteristics and the wear process can be compared.
- Effects of number of strokes: Examining the impact of increased number of stroke at a constant temperature can be done for the samples tested at 365 strokes to those at 3650 strokes, both at 75°C. This comparison was aimed at evaluating the effects of prolonged wear on the integrity and composition of the surface.

Figure 4.13a shows the surface of the counterbody, where, across the analyzed samples, three distinct lines are visible, along with particles detected in the gaps between these lines. These lines illustrate the load distribution at three separate points, and the material adhesion is observable within the spaces in-between. In figure 4.13b material addition was observed

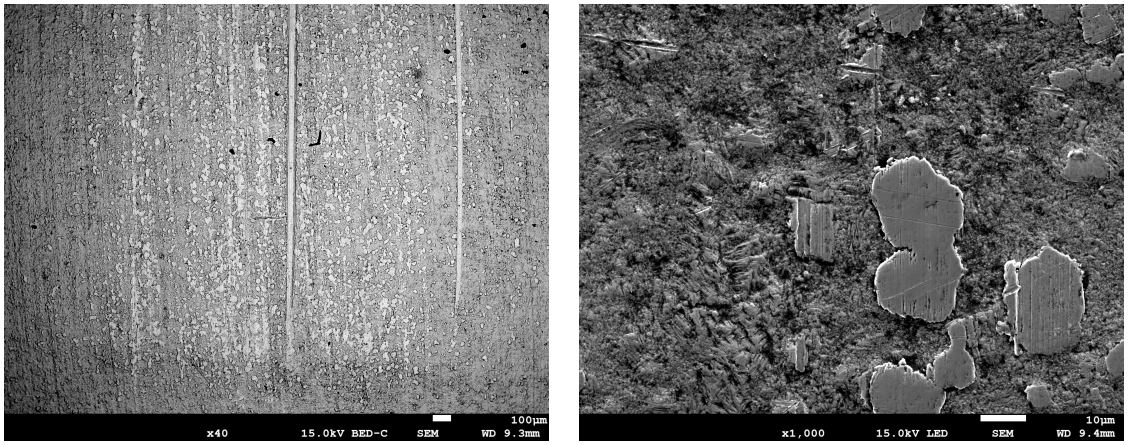


(A) x40 of the contact area

(B) x1000 on the particle in between the scratches

FIGURE 4.13: SEM images from the 365 number of strokes at 75 °C

Given that all the samples exhibited similar patterns, the areas featuring a scratch with particles were examined more closely at a magnification of x170. Figures 4.14a and 4.14b capture the effect of temperature increase. Observations from both figures revealed a consistent amount of particles present. However, figure 4.14b shows a more smooth surface compared to the other sample. This might be the effect of the higher temperature.

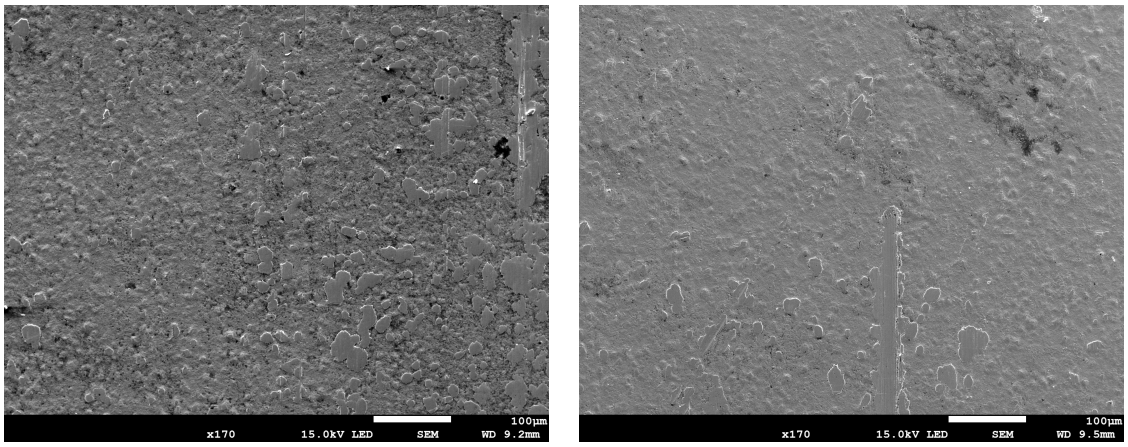


(A) 75°C

(B) 115°C

FIGURE 4.14: x170 for the 365 stroke with the temperature difference

Figure 4.15a, an x80 magnification of the 3650-stroke sample, shows an entirely blackened area with sharp particles visible along the line edges. Comparing this observation with figures 4.14a and 4.15b, it's evident that particles were present across all samples. However, the distinctive black coloration in the 3650-stroke sample is notable. This shows that the lubrication may have failed after multiple number of strokes and was deposited onto the surface. Despite cleaning efforts, the black marks persisted, indicating permanent alterations or damage to the surface due to extensive thermo chemical degradation.

The SEM observations did not reveal significant abnormalities on the surface. The scratch appeared consistent, and the particles displayed uniform structures. However, in the sample

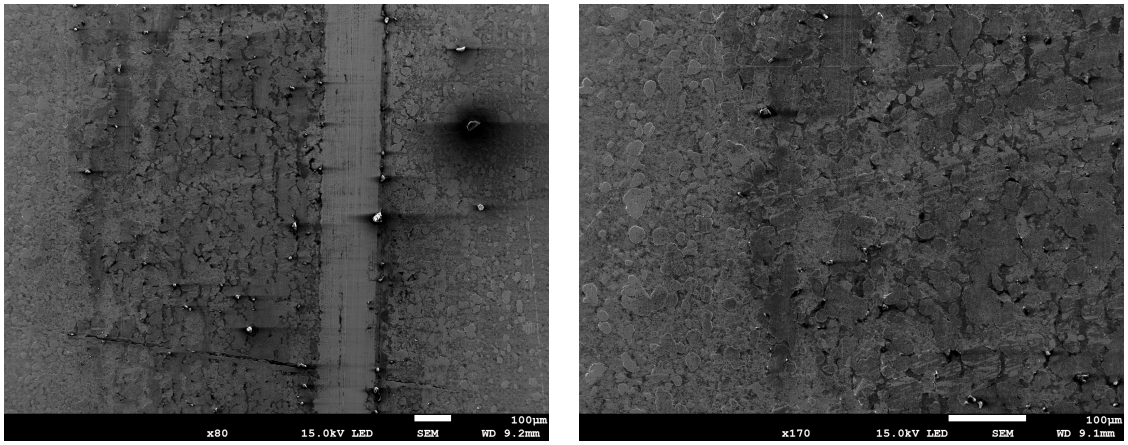


(A) x60 - focuses on the scratch and surroundings

(B) x170 - on the surface

FIGURE 4.15: SEM observation on 3650 strokes

subjected to 3650 strokes, sharp particles were noted along the edges, an finding that could be attributed to the wear and surface degradation resulting due to increase in number of strokes.

### 4.2.3 Elemental analysis

To further investigate, EDX analysis was employed subsequent to the SEM measurements. The purpose of the EDX was to identify the composition of the adhered material as well as to elucidate the nature of the black areas observed in the wear test with 3650 strokes.


FIGURE 4.16: Elemental analysis surface 365-75°C

The first elemental analysis was performed on an adhered wear particle (spectrum 1) and the surface area of an unworn part (spectrum 2) as shown in figure 4.16. The results for both spectra are shown in figure 4.17.

The results shows that the particle adhering to the surface was composed entirely of silver, indicating that material from the connecting rod had deposited onto this particular area.

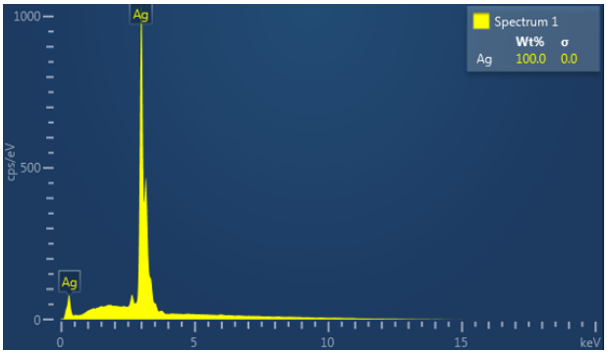


(A) Elemental analysis of spectrum 1

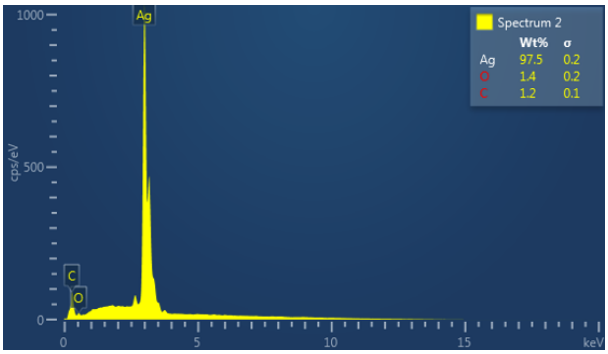


(B) Elemental analysis of spectrum 2

FIGURE 4.17: The results of the first elemental analysis for the number of stroke 365 and 75°C

However, the results of spectrum 2 highlighted the presence of oxide and carbon. This suggests that the material transfer resulted in a layer of pure silver on the surface, while also revealing signs of oxidation and carbon hinting at environmental interactions affecting the surface composition.

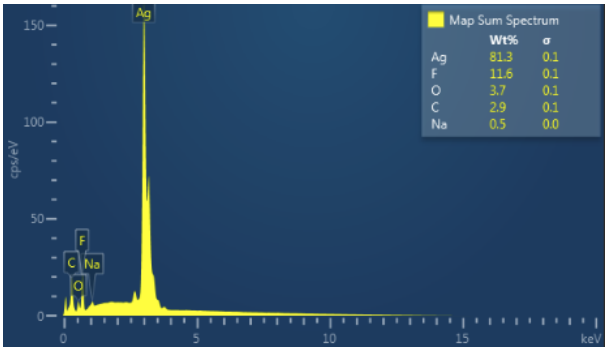


FIGURE 4.18: The result of the second elemental analysis for the 3650 stroke number region

The second elemental analysis focused on the region shown in figure 4.15a, with the results plot in figure 4.18. This analysis revealed a decrease in the presence of silver, along with the detection of elements like fluorine (F) and sodium (Na) on the surface. These elements are constituents of the lubricant used during the wear process and their presence on the surface suggests that residues from the lubrication remained after the testing.

# 5 Discussion

This chapter presents the discussion of the experimental results, focusing on three critical topics. Firstly, it discusses whether Archard's wear law can be met by the wear test results. Secondly, it discusses how the surface roughness have a potential impact on the ECR. Lastly, the chapter discusses effect of temperature on lubrication and wear of the contacting bodies.

## 5.1 Calculating wear volume due to adhesion

Assuming that the wear coefficient remains constant during the sliding, which helps to predict the lifespan of the component. Archard's equation shows the relation between the wear volume and the applied load and the sliding distance. For the connecting rod, an increase in the coating thickness was observed in specific contact regions, leading to its volume increase.


(A) Volume increase at the contact region

(B) The result of the elemental analysis of spectrum 2 for

FIGURE 5.1: Schematic of material addition on surface of cylinder due to adhesive wear.

Figure 5.1 shows the area where the thickness of the coating increases and how the volume at that specific contact can be calculated. For the calculation, it was considered that the increase in coating thickness is evenly distributed at the contact area. This means that the line contact area was used to calculate the cross section of this region.

To confirm Archard's wear law, the volumes per increase in coating thickness of the connecting rod per number of strokes were plotted using the linear fit plot. The slope of this linear plot calculates the wear coefficient for the increase in volume after the wear tests. Figure 5.2 shows the linear fit plot of the wear test results together with the mean volume of the number of storkes.

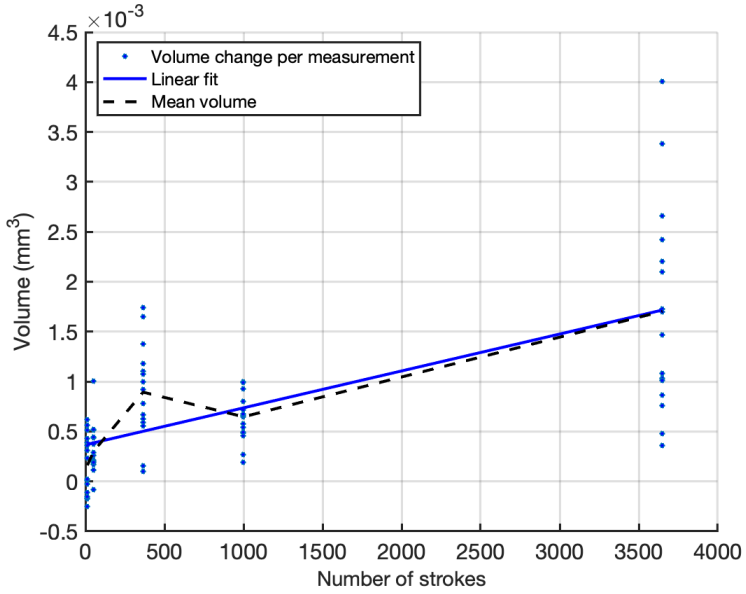


FIGURE 5.2: The volume increase vs the number of strokes at 75°C

The slope of the linear fit plot is $3.7 \times 10^{-7}$ $mm^3/(Nmm)$. A key observation from the plot is the significant variability evident across the data points, leading to a coefficient of determination of only 43.67%. Additionally, the mean volume per stroke number is plotted, but does not show any linear relationship with an increasing number of strokes. Consequently, it can be concluded that the results do not conform to Archard's law.

Figure 4.9 shows that 12 and 52 strokes can be considered as the initial run-in phase of wear, characterized by a notable increase in thickness. When comparing these early stages with the 365 and 1000 strokes, it is obvious that the initial stages start with a significant thickness increase. The 365 and 1000 strokes represent the transition into a steady state phase of wear. However, when evaluating against the 3650 strokes, the thickness increase is observed to double. The 3650 stroke phase can be classified as accelerated wear as shown in stage III in figure 1.8 due to the presence of thermo chemical wear as observed form the elemental analysis in section 4.2.3.

## 5.2 Electrical contact resistance of the tribological system

Figure 5.3 shows a schematic overview to show the interaction between the connecting rod and the silver coated plate after the wear test. In between the connecting rod and the plate, a red region is shown as the thickness increase of the coating($\delta$z) on the connecting rod. To discuss the effect of wear on the ECR of the connecting rod and tulip, equation (1.2) was adjusted to equation (5.1). The electrical resistivity of the material ($\rho$), the length of the equation has been substituted with $\delta$z and the real contact area (Ar).

$$ECR = \rho \cdot \left( \frac{\Delta z}{A_r} \right) \tag{5.1}$$

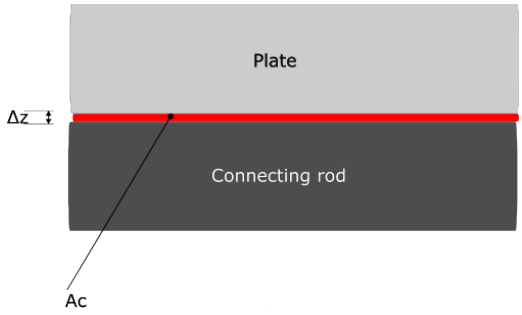


FIGURE 5.3: Schematic of the contacting interfaces of the connecting rod and plate after the wear test

The function of the surface roughness measurements, using the Ra and Rq values, obtained in section 4.1.2. The distribution of the mean Ra values follows a Gaussian distribution, as shown in figure 5.4, with the Rq values serving as the standard deviation.

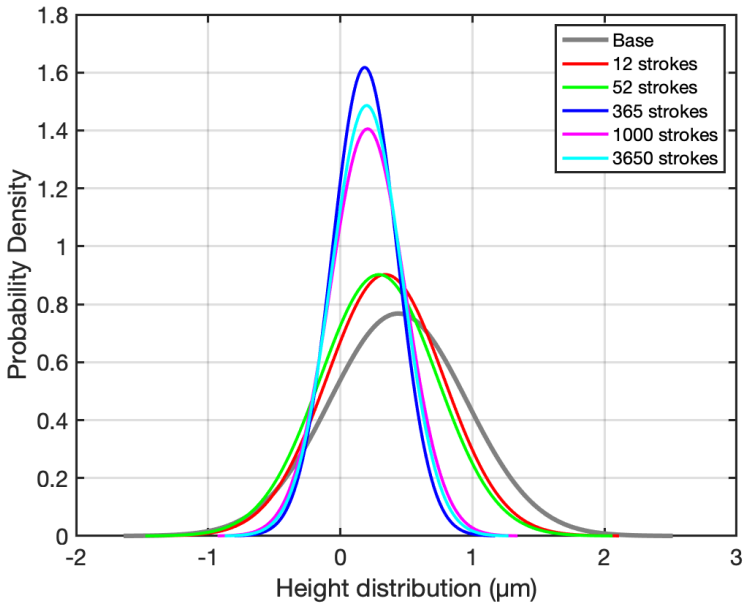


FIGURE 5.4: The Gaussian distribution performed after the wear test at different strokes using the Ra and Rq values

The Gaussian distribution demonstrates that a higher peak and a less spread-out plot, indicating a smaller Rq, result in smoother surfaces. Also, the ends of the distributions also show significant changes, with the right end shrinking from around 2.5 µm to approximately 0.5 µm and the left end close to 0 as stroke frequency increases. This indicates that the highest asperities are being effectively smoothed out, further contributing to a increase in the real contact area between surfaces. This reduction in the real contact area is expected to decrease the ECR.

The wear test results from the tribological system, which contains the connecting rod and silver coated plate, showed that adhesive wear was the predominant wear mechanism. The surface roughness of the connecting rod was decreased and the surface roughness of the

silver coated plate increased, which showed 100% silver lumps. According to [22] and [23], the initial surface contact area will change and since the asperities are just in contact between the bodies, does this mean that the initial contact area will decrease. If the $Ar$ in equation (5.1) decreases, the the ECR will increase. The decrease of the contact area, which resulted in the increase of the ECR was also explained in [29].

To translate the results from the test configuration into the connector mechanism might be different. There are some differences despite using the same contact pressure, materials, and environmental influences. The primary difference arises from the design differences in the contact interfaces. Specifically, the current design of the tulip surface, which feature grooves, which are absent in the silver-coated plate used in the tests. This discrepancy exists because the plate was already coated prior to any attempt to replicate the textured surface of the tulip section onto the plate. This difference in surface texture between the test plate and actual tulip contacts is significant, as it could affect the overall behavior and performance of the connector mechanism.

The anticipated wear mechanism that occurs between the connecting rod and the tulip is expected to be the same as that of the cylinder on the plate configuration previously tested. In both scenarios, the materials are the same, which means that there is no difference in the hardness and only adhesive wear is dominated. The main reason for the adhesive wear is that in the same metals a strong adhesive bond is formed. The material strength The formation of adhesive wear particles occurs when weaker paths within the material fail while adjacent to a stronger interface [48, 49]. In the wear tests, the silver coated plate is flat and roughens up transferring material to the connecting rod and increase its coating thickness after initial smoothing. However, in the connector mechanism, it is anticipated that both the connecting rod and the tulip grooves will smooth out to the point where the grooves are reduced and some lumps are formed at both components. Consequently, there will be no coating thickness increase in any particular specimen.

In the case of the connector mechanism,the contact area initially increases as the surface smooths, which is shown in the Gaussian plot. However, it decreases once lumps begin to form. Consequently, the ECR will decrease initially but then increase later in the process. Ideally, a consistent ECR is desired.

## 5.3 Effect of temperature on lubrication and wear

The viscosity results from section 3.2, must be converted to dynamic viscosity by calculating those values with the density of the lubricant. Table 5.1 listed the dynamic viscosity, which will be used instead of the base viscosity in equation (3.2).

TABLE 5.1: Dynamic Viscosity at Various Temperatures

| **Temperature (°C)** | **Dynamic Viscosity (mPa·s)** |
|---|---|
| 20 | 901.6 |
| 50 | 166.6 |
| 75 | 49.0 |
| 115 | 11.8 |

Each lambda ratio for 365 strokes was calculated and plotted in figure 5.5.

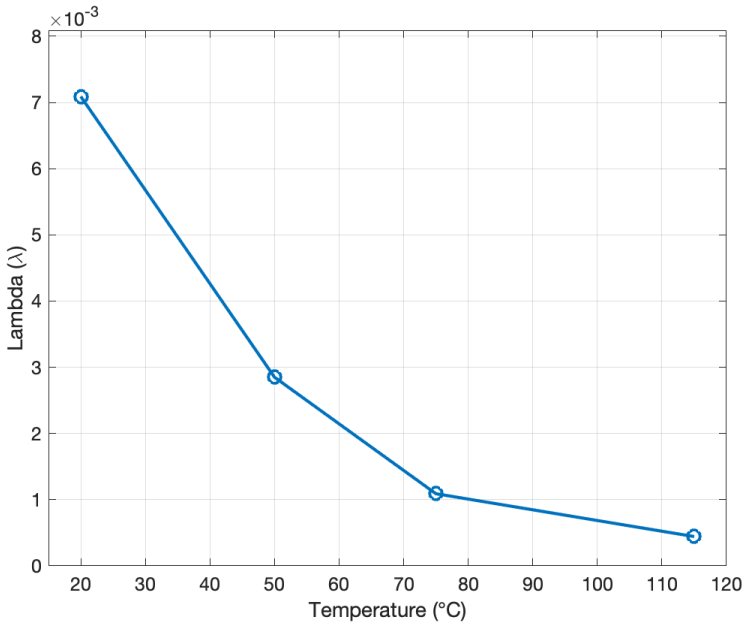


FIGURE 5.5: Lamda ratio vs temperature at 365 strokes

The consistently decreasing $\lambda$ ratio below 1 across increasing the temperatures, confirms that the system consistently operates within the boundary lubrication regime and that the lubrication is insufficient, as explained in [33]. In this regime, the lubricant film is too thin to prevent direct contact between surfaces, leading to higher friction and increased wear risk. With an increase in temperature, the thickness of the lubrication decreases significantly. This assertion is further supported by the observation that the surface roughness of the connecting rod decreases immediately with a lower number of strokes, indicating that the temperature primarily affects the lubricant.

In the wear test, the impact of temperature on thermal expansion is demonstrated by the behavior of the silver coating on the plate, which has a coefficient of thermal expansion of $20 \times 10^{-6}/°C$. This rate is higher than that of copper at $16 \times 10^{-6}/°C$, and higher than the base material (probably steel) to which the silver plate is fixed. As a result, with increasing temperatures, the silver-coated plate will act like a bimetallic strip and bend out of the contact. This bending reduces both the conformity and the contact area, with more sever contact. Though this effect is not significant, it is still present. The circular spring in the connector mechanism is made of steel, which means that as temperatures rise, there will be increased compression on the tulip, resulting in more stress [50, 51].

# 6 Conclusion and recommendation

In this thesis, the contact and operating conditions of the connector mechanism were simulated using a cylinder on plate test configuration. The study revealed that the adhesive wear mechanism significantly affects the lifetime of the connector mechanism, becoming the dominant wear mode with increasing sliding distance and operating time. During this period, the contact area between the contacting bodies of the connecting rod and plate decreased. This was primarily due to material transfer from the plate to the cylinder due to adhesion, which led to the formation of lumps on the surface of the cylinder which increased roughness of the plate in return. The lumps also locally changed the curvature of the cylinder and reduced the area of the nominally flat line contact.

The decrease in contact area, coupled with the increase in coating thickness at localized points due to the lumps, is directly linked to the increase of the ECR, that detrimentally impacts the systems service life. Notably, the lubricant applied during the tests failed to the thermal effects over extended operation periods and remained within the boundary lubrication regime and decreased even more. This suggests that to delay or prevent wear by avoiding metal-to-metal contact, an alternative lubrication strategy is required. However, it is important to note that even though the lubricant did not fully prevent adhesive wear, the 10$\mu$m coating thickness was thick enough to ensure that the substrate copper was not exposed to the environment.

## 6.1 Recommendations

In this section, the recommendations regarding to this research is explained. The recommendations consists of changes what could be make in the test configurations, but also further research.

The first recommendation is make adjustments to the test configuration. In the case of both the connecting rod and the silver coated plate, the surface roughness measurements revealed significantly large error bars, due to the non uniform distribution of wear tracks within the contact area. Instead of isolating changes to specific regions of contact measurements encompassed the entire line contact, contributing to the observed discrepancies in the wear measurement. These discrepancies were further compounded by using the actual connecting rod of the mechanism as the test cylinder as the radius of the rod and the surface characteristics varied in all tests. Additionally, misalignment within the line contact significantly influenced the results, as outlined in section 4.1.1. These challenges could potentially be mitigated by employing a cylinder designed with a flatter surface and controllable geometrical parameters such as radius, length and profile. This approach could

likely minimize the bending effects on the silver-coated plate, offering more uniformly distributed wear tracks.

Another recommendation is to conduct wear tests by first aging the current lubricant to evaluate the impact on wear rates and longevity. Considering that the lubricant in the connector mechanism can remain for up to 50 years, they will inevitably age. The aging of lubricant could yield results that vary significantly from those obtained in this study. In the following study [39], it was found that an aged synthetic oil affects contact wear.

Another valuable are of research is to explore the use of Teflon/fluorine free lubricants, especially given the potential EU regulations [52] banning fluorine and Teflon based lubricants, which significantly affect all the current switchgears in service. The existing test setup from the wear tests can be adapted to test different lubricants and assess their impact on wear. Conducting this study would aid in identifying suitable alternative lubricants that adhere to new regulations and ensure the optimal performance and durability of switchgear components under operational conditions.

To minimize the adhesive wear in the connector mechanism, it can be investigated if it is possible to use dissimilar coating to prevent the adhesive wear. However, it is important to keep the hardness difference in both coatings minimal to avoid the possibility of abrasive wear, which can occur if one of the materials is harder. Another investigation is to use more durable lubrication, which is able to reduce the direct contact between the surfaces and keep it in the full lubrication regime.

# Bibliography


[1] Boston University. Electricity and circuits. https://www.bu.edu/lernet/artemis/years/2011/slides/circuits.pdf, 2011.

[2] B Thalheim. Models, to model, and modelling—towards a theory of models, especially conceptual models and modelling. *Collection of Papers*, pages 2020–2021, 2020.

[3] Eaton. Fundamentals of medium voltage switchgear. https://www.eaton.com/us/en-us/products/medium-voltage-power-distribution-control-systems/switchgear/fundamentals-of-medium-voltage-switchgear.html, 2023.

[4] ASCO Power Technologies. What is switchgear? https://www.ascopower.com/us/en/resources/articles/what-is-switchgear.jsp, 2023.

[5] R Chennakeshava, R Niharika Rao, M Karthik, S Mohammed, and R Prajath Mahabala. A review on switchgear analysis and common challenges observed in switchgear. *IJERT*, 10:4, 2021.

[6] Aravinth Subramaniam, Animesh Sahoo, Sai Srinivas Manohar, Santosh Raman, and Sanjib Panda. Switchgear condition assessment and lifecycle management: Standards, failure statistics, condition assessment, partial discharge analysis, maintenance approaches, and future trends. *IEEE Electrical Insulation Magazine*, 37:27–41, 04 2021.

[7] N. K. Myshkin. Tribological problems in electrical contacts. *Tribology International*, 24(1):45–49, 1991.

[8] A Carvalho, ML Cormenzana, H Furuta, W Grieshaber, A Hyrczak, D Kopejtkova, JG Krone, M Kudoke, D Makareinis, JF Martins, et al. Final report of the 2004–2007 international enquiry on reliability of high voltage equipment. *Electra (Paris)*, 264:49–53, 2012.

[9] Zhengfeng Cao, Yanqiu Xia, Chuan Chen, Kai Zheng, and Yi Zhang. A synergetic strategy based on laser surface texturing and lubricating grease for improving the tribological and electrical properties of ag coating under current-carrying friction. *Friction*, 9:978–989, 2021.

[10] Dipl.-Ing. Jürgen Dreier. Quality of electrical connections in power distribution. Technical report, KoCoS Messtechnik AG, Korbach, Germany, July 2019. Product Manager KoCoS Messtechnik AG.

[11] IEC 62271-200. High-voltage switchgear and controlgear–part 200: Ac metal-enclosed switchgear and controlgear for rated voltages above 1 kv and up to and including 52 kv. 2011.

[12] Dieter König. The role of vacuum in circuit breaker technology. In *2012 25th International Symposium on Discharges and Electrical Insulation in Vacuum (ISDEIV)*, pages A1–A14. IEEE, 2012.

[13] Eaton Corporation. Vacuum_gs_aant-pres. PowerPoint presentation, 2002.

[14] International Electrotechnical Commission et al. Iec 62271-1: 2007. high-voltage switchgear and controlgear-part 1: Common specifications. *International Electrotechnical Commission*, page 252, 2007.

[15] *Fundamentals of Wear Failures*. ASM International.

[16] What is wear - definition | material properties. https://material-properties.org/what-is-wear-types-classification-and-differences-definition/, 2023. Accessed: 2024-01-04.

[17] Pranay Kumar. Wear. https://www.tribonet.org/wiki/wear/, 5 2022.

[18] Saad M. S. Mukras. Computer simulation/prediction of wear in mechanical components. *Advances in Tribology*, 2020:15, 2020.

[19] Andrea la Monaca, James Murray, Zhirong Liao, Alistair Speidel, José Robles Linares Alvelais, Dragos Axinte, Mark Hardy, and Adam Clare. Surface integrity in metal machining - part ii: Functional performance. *International Journal of Machine Tools and Manufacture*, 03 2021.

[20] JeFoa Archard. Contact and rubbing of flat surfaces. *Journal of applied physics*, 24(8):981–988, 1953.

[21] Michael Varenberg. Adjusting for running-in: Extension of the archard wear equation. *Tribology Letters*, 70(2):59, 2022.

[22] Bojan Podgornik. Adhesive wear failures. *Journal of Failure Analysis and Prevention*, 22(1):113–138, 2022.

[23] Morton Antler. Tribology of metal coatings for electrical contacts. *Thin solid films*, 84(3):245–256, 1981.

[24] Satyadeo Vyas. Electrical contact resistance and its importance. https://www.electricalvolt.com/electrical-contact-resistance-its-importance/, 2022.

[25] Jian Song and Vitali Schinow. Correlation between friction and wear properties and electrical performance of silver coated electrical connectors. *Wear*, 330:400–405, 2015.

[26] Haomiao Yuan, Jian Song, and Vitali Schinow. Simulation methodology for prediction of the wear on silver-coated electrical contacts with a sphere/flat configuration. *IEEE Transactions on Components, Packaging and Manufacturing Technology*, 8(3):364–374, 2017.

[27] Robert L Jackson, W Robert Ashurst, George T Flowers, Santosh Angadi, Song-yul Choe, and Michael J Bozack. The effect of initial connector insertions on electrical contact resistance. In *Electrical Contacts-2007 Proceedings of the 53rd IEEE Holm Conference on Electrical Contacts*, pages 17–24. IEEE, 2007.

[28] James A Greenwood and JB Pl Williamson. Contact of nominally flat surfaces. *Proceedings of the royal society of London. Series A. Mathematical and physical sciences*, 295(1442):300–319, 1966.

[29] Sujoy Talukder, Chang-Dong Yeo, Yang-Ki Hong, Minyeong Choi, Robert C Flicek, and Joseph E Bishop. Analytical modeling and simulation of electrical contact resistance for elastic rough electrode surface contact including frictional temperature rise. *AIP Advances*, 12(2), 2022.

[30] Chongpu Zhai, Dorian Hanaor, Gwénaëlle Proust, and Yixiang Gan. Stress-dependent electrical contact resistance at fractal rough surfaces. *Journal of Engineering Mechanics*, 143(3):B4015001, 2017.

[31] Dongwei Wang, Xiao Chen, Faqiang Li, Bo Wan, Bin Liu, Yang Zhao, and Xianguo Qing. Effect of surface texture on the tribological behavior of sliding electrical contact interface. *Surface Topography: Metrology and Properties*, 11(2):025008, 2023.

[32] Manoj Rajankunte Mahadeshwara. Elastohydrodynamic lubrication (ehl): Theory and definition. https://www.tribonet.org/wiki/elastohydrodynamic-lubrication-ehl/, February 2017.

[33] Tribonet. Stribeck curve - tribology encyclopedia. https://www.tribonet.org/wiki/stribeck-curve/, 2024.

[34] Justin Michaud. Lambda ratio. *Gear Solutions*, OCT 2016.

[35] Josephine Kelley, Kambiz Babaalihaghighi, Norbert Bader, Christian Wege, Florian Pape, and Gerhard Poll. Application of hertzian theory to torus on plane contacts. *Proceedings of the Institution of Mechanical Engineers, Part J: Journal of Engineering Tribology*, 236:2189–2208, 2022.

[36] Evan Drumwright. A fast and stable penalty method for rigid body simulation. *IEEE transactions on visualization and computer graphics*, 14:231–40, 01 2008.

[37] Engineering ToolBox. Poisson's ratios metals. https://www.engineeringtoolbox.com/metals-poissons-ratio-d_1268.html, 2007.

[38] Klüber Lubrication. BARRIERTA L 55/2 - High-temperature long-term grease. https://www.klueber.com/us/en/products-service/products/barrierta-l-55-2/9880/.

[39] Pantelis G Nikolakopoulos, Stamatis Mavroudis, and Anastasios Zavos. Lubrication performance of engine commercial oils with different performance levels: The effect of engine synthetic oil aging on piston ring tribology under real engine conditions. *Lubricants*, 6(4):90, 2018.

[40] Max Marian, Marcel Bartz, Sandro Wartzack, and Andreas Rosenkranz. Non-dimensional groups, film thickness equations and correction factors for elastohydrodynamic lubrication: A review. *Lubricants*, 8(10):95, 2020.

[41] Emircan Özçelikci, Hüseyin İlcan, Gürkan Yıldırım, and Mustafa Şahmaran. *11 - Nanoscale characterization of cementitious composites*. Woodhead Publishing Series in Civil and Structural Engineering. Woodhead Publishing, 2022.

[42] Warren Carl Oliver and George Mathews Pharr. An improved technique for determining hardness and elastic modulus using load and displacement sensing indentation experiments. *Journal of materials research*, 7(6):1564–1583, 1992.

[43] Anton Paar Wiki. Instrumented indentation testing (iit). https://wiki.anton-paar.com/en/instrumented-indentation-testing-iit/, 2024.

[44] J. Goldstein, Dale Newbury, David Joy, Charles Lyman, Patrick Echlin, Eric Lifshin, Linda Sawyer, and Joseph Michael. *Scanning Electron Microscopy and X-ray Microanalysis ISBN: 0306472929*, volume XIX. 01 2003.

[45] Rene Van Grieken and Andrzej Markowicz. *Handbook of X-ray Spectrometry*. CRC press, 2001.

[46] Althen Sensors. Fujifilm Measurement Foils Fujifilm Prescale. https://www.althensensors.com/uploads/products/datasheets/fujifilm-measurement-foils-fujifilm-prescale-en.pdf, 2024.

[47] Bruker Corporation. Umt tribolab. https://www.bruker.com/en/products-and-solutions/test-and-measurement/tribometers-and-mechanical-testers/umt-tribolab.html, 2024.

[48] TW Scharf and SV Prasad. Solid lubricants: a review. *Journal of materials science*, 48:511–531, 2013.

[49] Ernest Rabinowicz. An adhesive wear model based on variations in strength values. *Wear*, 63(1):175–181, 1980.

[50] The Engineering Toolbox. Linear expansion coefficients. https://www.engineeringtoolbox.com/linear-expansion-coefficients-d_95.html, 2024.

[51] The Engineering Toolbox. Heat and bending of bimetallic strips. https://www.engineeringtoolbox.com/bimetallic-strips-d_1755.html, 2024.

[52] Adrian Mota-Babiloni and Pavel Makhnatch. Predictions of european refrigerants place on the market following f-gas regulation restrictions. *International Journal of Refrigeration*, 127:101–110, 2021.

# Appendix

# Appendix A: Circular spring test

The circular spring test was conducted due to the insufficient information from the supplier; only the material and dimensions of the spring were provided. The desired spring constant, which was crucial for the calculations in section 2.3.2, was unknown. Additionally, the circular spring operated in the radial direction, complicating the measurement process.

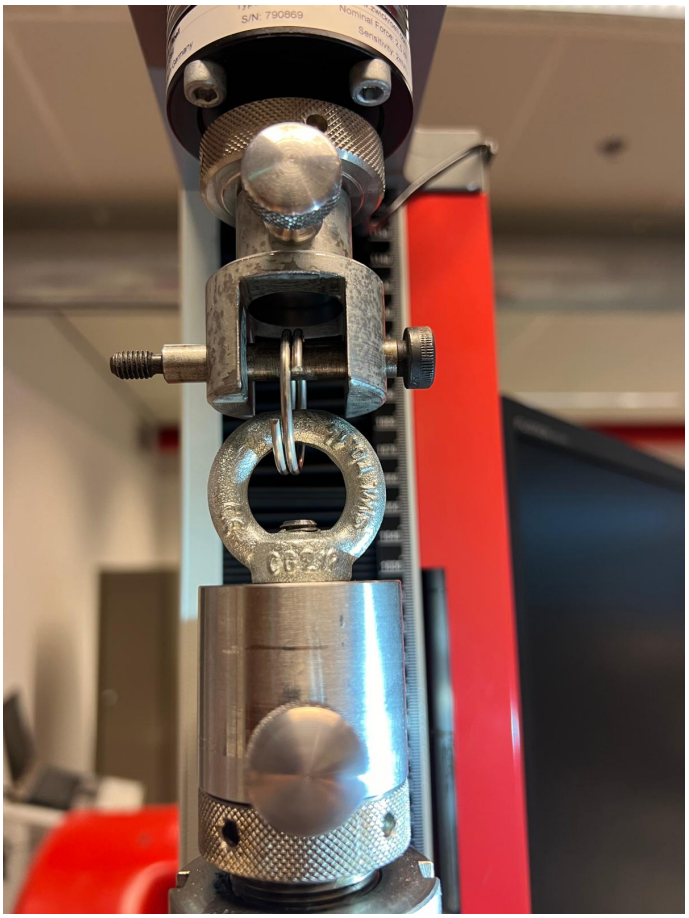

FIGURE .1: Force vs travel of the circular spring using the tensile bar

The testing setup used for the circular spring test was identical to the performance test described in section 3.4. However, in this setup, the connecting rod and tulip were replaced with the circular spring, which was positioned using a lifting eye and a bolt, see figure .1. The lifting eye moves downward with a velocity of 10 mm/s.

According to the supplier's specifications, the circular spring can expand up to 1.5 mm in diameter. During the test, the lifting eye extended the spring to a maximum of 1.3 mm. This extension was measured and presented in figure .2.

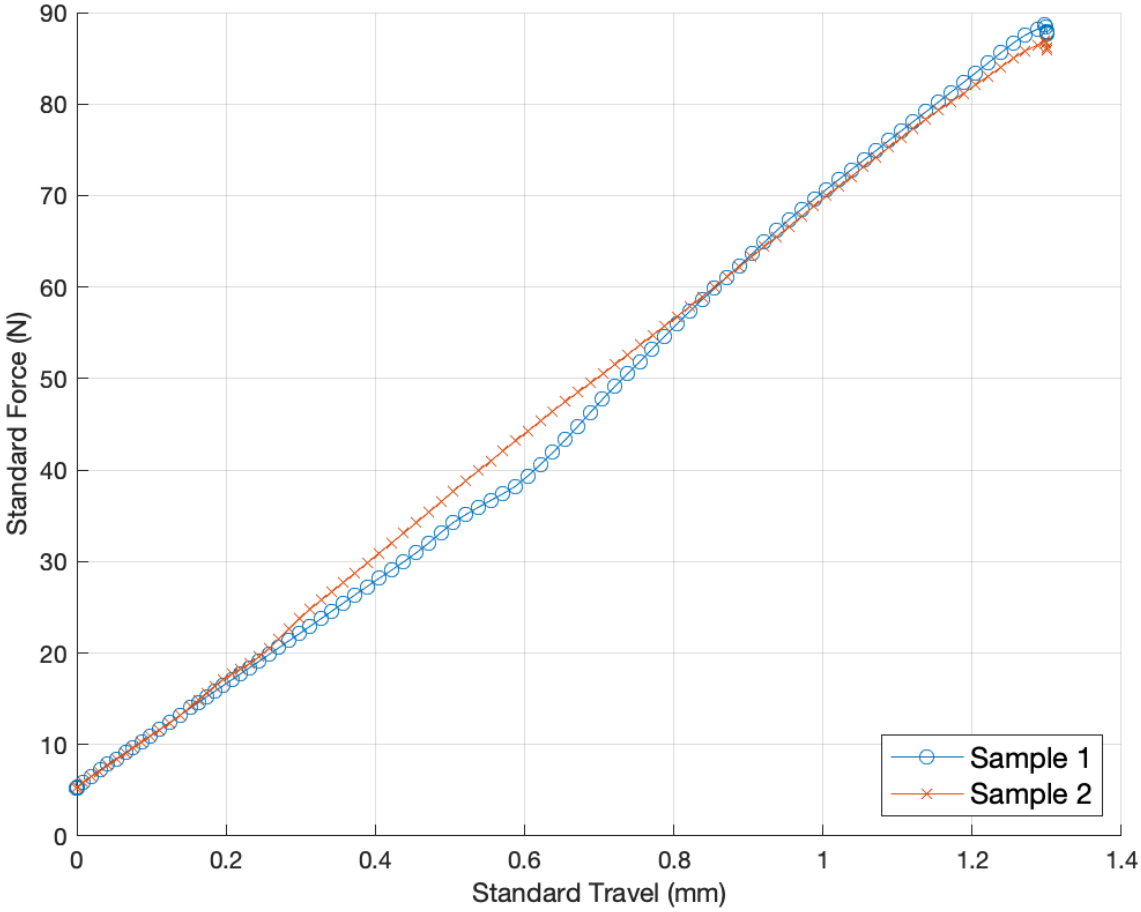


FIGURE .2: The Standard travel against the standard force for two samples at a specific position

The plot for the two samples appears to be nearly identical. To calculate the spring constant, the selected force must be multiplied by the corresponding displacement.

## Appendix B: Performance test

During the performance test, measurements were taken from two samples. Figure .3 presents the raw data collected from these measurements. A key observation from the analysis is the notable difference between the samples. When compared at identical velocities, it is evident that Sample 2 exhibits a higher maximum force than Sample 1. Additionally, bumps were consistently observed post-bending in all measurements. It is also worth noting that the values at 10 mm/s and 5 mm/s velocities are similar, whereas the values significantly decrease at the lowest velocity. Due to the significant differences

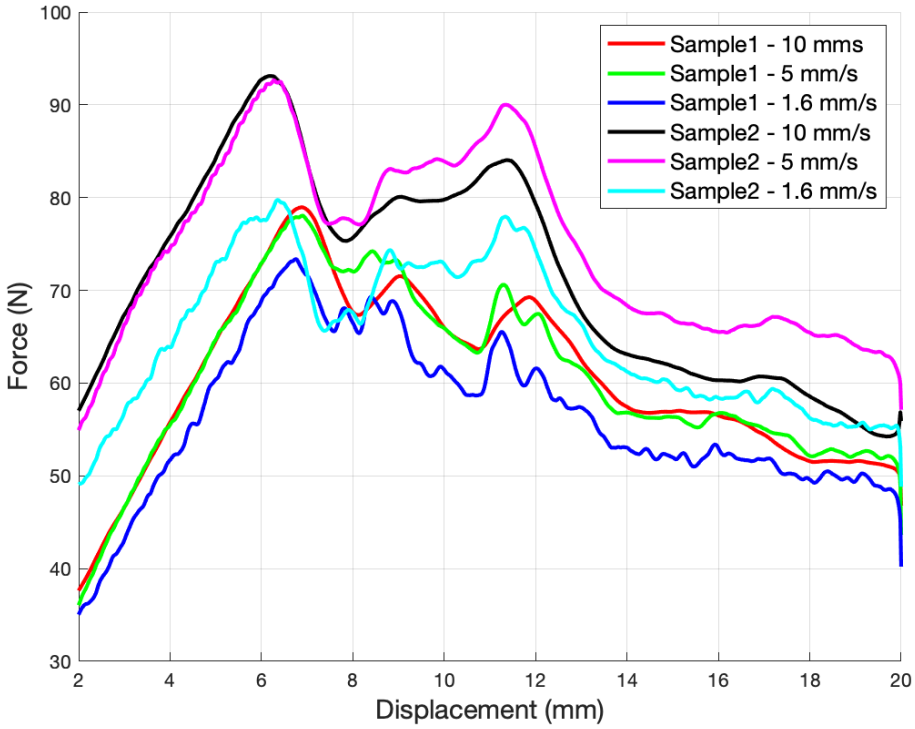


FIGURE .3: The results of the performance tests at different velocities

observed between the initial samples, two new samples were introduced and exclusively measured at a velocity of 10 mm/s. The results from these measurements are detailed in section 3.4.

# Appendix C: Friction test

The results at friction speeds of 1.6 mm/s and 5 mm/s are shown in Figure .4a and Figure .4b, respectively. When compared to the results at 10 mm/s, explained in section 3.5.1, these results exhibit smaller error bars and are more closely aligned.

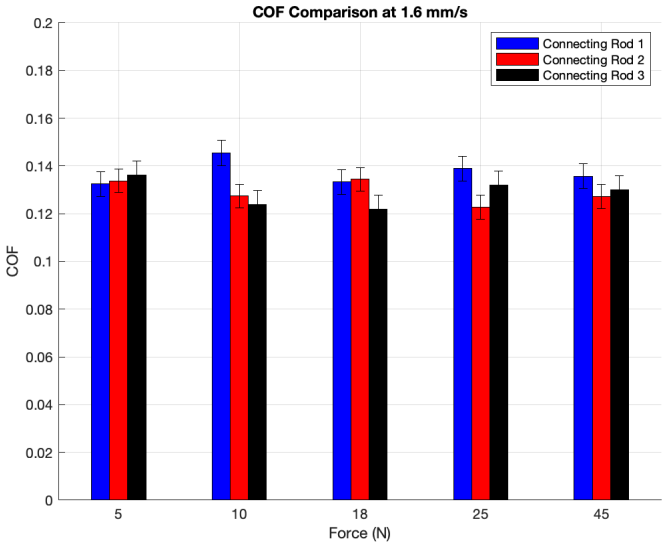


(A) COF comparison at 1.6 mm/s

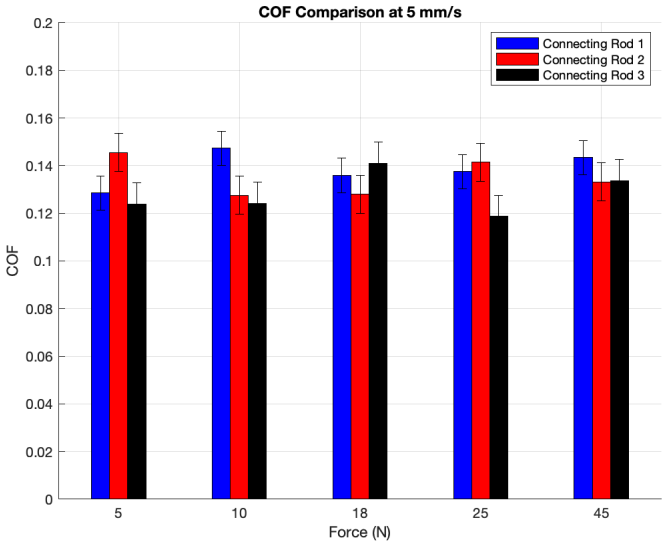


(B) COF comparison at 5 mm/s

FIGURE .4: The COF results obtained from the friction test on three connecting rods

## Appendix D: Confocal images and results of worn surface

The appendix includes confocal images of the worn surfaces for both the connecting rod and the silver coated plate. Figure .5 and figure .6 shows the confocal images of the two samples for 365 number of strokes and 75 °C. The method explained in section 4.1.2 was used to measure the surface roughness values.

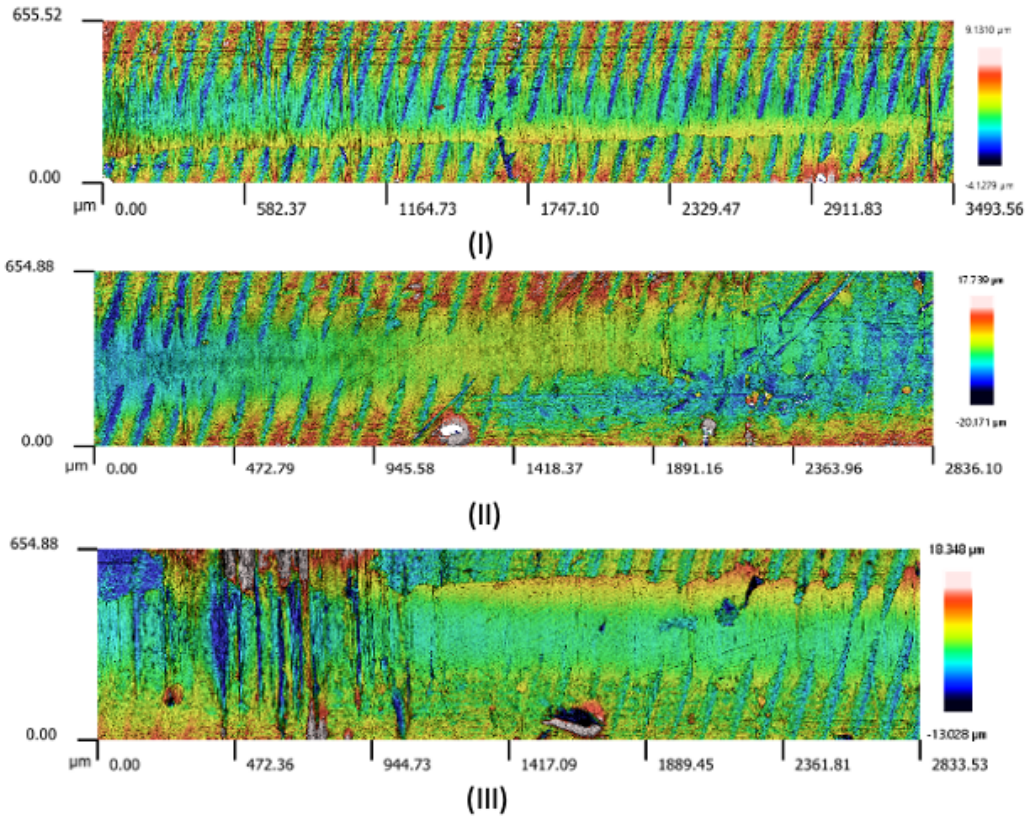


FIGURE .5: The confocal images of sample 1 for 365 number of strokes at 75 °C. (I) left section, (II) middle section and (III) right section of the connecting rod

The data clearly shows that wear occurs in patches across the entire contact area. The measurements for surface roughness are provided in Table .1 for the Ra values and in Table .2 for the Rq values. The notation in the tables, such as Ra1L, Ra1M, and Ra1R, indicates specific measurements: the numeral represents the measurement instance, while the letters L, M, and R designate the left, middle, and right sections of the contact area, respectively. Each section includes three separate measurements.

Figure .7 and figure .8 shows the confocal images of the silver coated plate following the

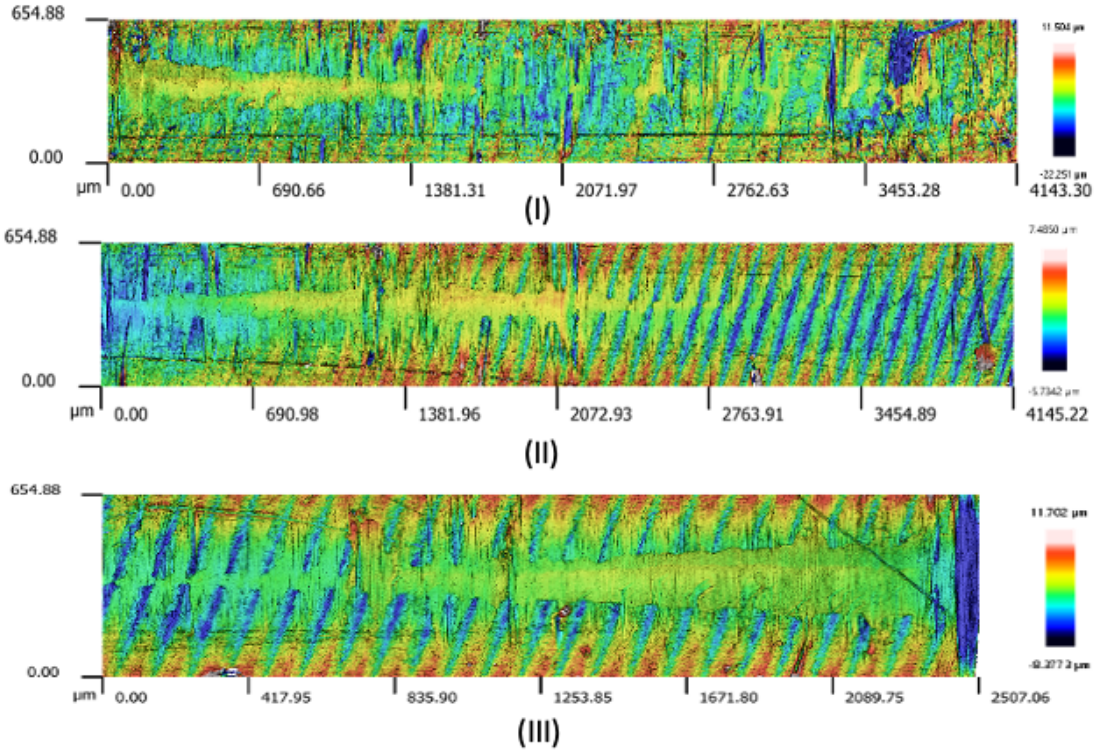


FIGURE .6: The confocal images of sample 2 for 365 number of strokes at 75 °C. (I) left section, (II) middle section and (III) right section of the connecting rod

TABLE .1: The Ra values after the wear test on the connecting rod

| Sample | Stroke | Temp | Ra1L | Ra2L | Ra3L | Ra1M | Ra2M | Ra3M | Ra1R | Ra2R | Ra3R | Mean | STD |
|---|---|---|---|---|---|---|---|---|---|---|---|---|---|
| 1 | 12 | 75 | 0.3026 | 0.2474 | 0.3342 | 0.2051 | - | 0.5364 | 0.4161 | 0.4208 | 0.3314 | 0.3493 | 0.1059 |
| 1 | 52 | 75 | 0.3850 | 0.1315 | 0.2901 | 0.1536 | 0.2422 | 0.2587 | 0.3529 | 0.3251 | 0.3352 | 0.2749 | 0.0875 |
| 1 | 365 | 75 | 0.1484 | 0.1489 | 0.1873 | 0.2853 | 0.1393 | 0.3217 | - | 0.1130 | 0.1258 | 0.1837 | 0.0776 |
| 1 | 1000 | 75 | 0.1257 | 0.1655 | 0.1823 | 0.3042 | 0.2128 | - | 0.2202 | 0.1749 | 0.1527 | 0.1923 | 0.0546 |
| 1 | 365 | 20 | 0.2243 | 0.1611 | 0.2117 | 0.1688 | 0.1168 | 0.2294 | 0.3292 | 0.3361 | 0.2447 | 0.2247 | 0.0731 |
| 1 | 365 | 50 | 0.1180 | 0.0743 | 0.1160 | 0.1535 | 0.1223 | 0.1306 | 0.0917 | 0.0717 | 0.0993 | 0.1086 | 0.0268 |
| 1 | 365 | 115 | 0.1379 | 0.2626 | 0.1087 | 0.0836 | 0.1245 | 0.0840 | 0.1017 | 0.0798 | 0.1155 | 0.1220 | 0.0563 |
| 1 | 3650 | 75 | 0.3362 | 0.1236 | - | 0.3581 | 0.1229 | 0.1496 | 0.1939 | 0.1684 | 0.3435 | 0.2245 | 0.1033 |
| 1 | 1000 | 115 | 0.1092 | 0.1598 | 0.1184 | 0.2874 | 0.0980 | 0.1503 | 0.1323 | 0.1247 | 0.1447 | 0.1472 | 0.0562 |
| 2 | 12 | 75 | 0.3737 | 0.2029 | 0.2880 | 0.2675 | 0.3959 | - | 0.3608 | 0.3536 | 0.4108 | 0.3317 | 0.0672 |
| 2 | 52 | 75 | 0.3999 | 0.3978 | 0.4236 | 0.3522 | 0.3537 | 0.3495 | 0.1479 | 0.2160 | 0.1377 | 0.3087 | 0.1047 |
| 2 | 365 | 75 | 0.1007 | 0.2560 | 0.2771 | 0.2474 | 0.1975 | - | 0.2052 | 0.0984 | 0.0918 | 0.1843 | 0.0718 |
| 2 | 1000 | 75 | 0.1884 | 0.2882 | 0.3195 | 0.1726 | 0.0893 | 0.1966 | 0.2784 | 0.0764 | 0.3689 | 0.2198 | 0.0952 |
| 2 | 365 | 20 | 0.1595 | 0.1783 | 0.1506 | 0.2474 | 0.1053 | 0.3963 | 0.2879 | 0.2838 | - | 0.2261 | 0.0892 |
| 2 | 365 | 50 | - | 0.2578 | 0.1830 | 0.2030 | 0.3337 | 0.1722 | 0.2278 | 0.2110 | 0.2109 | 0.2249 | 0.0479 |
| 2 | 365 | 115 | 0.1164 | 0.0739 | 0.0571 | 0.1171 | 0.2345 | 0.1421 | 0.1973 | 0.3110 | 0.3444 | 0.1771 | 0.0961 |
| 2 | 3650 | 75 | 0.2375 | 0.2088 | 0.1637 | 0.2213 | 0.1177 | 0.0977 | 0.1629 | 0.1833 | 0.1623 | 0.1728 | 0.0433 |
| 2 | 1000 | 115 | 0.0740 | 0.1601 | 0.1895 | 0.0632 | 0.1029 | 0.0832 | 0.1313 | 0.0658 | 0.0735 | 0.1048 | 0.0429 |

wear test. As described in Section 4.2.1, the images were split into two to capture the entire contacting area.

The results of the surface roughness is listed in table .3.The notation in the table, such as RaR and RqL, indicates specific measurements: the letter L and R designate left and right sections of the contact area.

TABLE .2: The Rq values after the wear test on the connecting rod

| Sample | Stroke | Temp °C | Ra1L | Ra2L | Ra3L | Ra1M | Ra2M | Ra3M | Ra1R | Ra2R | Ra3R | Mean $\mu$m | STD $\mu$m |
|---|---|---|---|---|---|---|---|---|---|---|---|---|---|
| 1 | 12 | 75 | 0.3901 | 0.3584 | 0.4152 | 0.3007 | - | 0.6575 | 0.5529 | 0.5242 | 0.4160 | 0.4519 | 0.1170 |
| 1 | 52 | 75 | 0.4455 | 0.1778 | 0.3514 | 0.2129 | 0.2907 | 0.3105 | 0.4479 | 0.3945 | 0.4206 | 0.3391 | 0.0988 |
| 1 | 365 | 75 | 0.2003 | 0.2310 | 0.3021 | 0.3364 | 0.2038 | 0.4145 | - | 0.1787 | 0.1809 | 0.2560 | 0.0860 |
| 1 | 1000 | 75 | 0.1649 | 0.2377 | 0.2278 | 0.4641 | 0.2588 | - | 0.3200 | 0.2486 | 0.2109 | 0.2666 | 0.0910 |
| 1 | 365 | 20 | 0.4263 | 0.2142 | 0.2684 | 0.2014 | 0.1588 | 0.3637 | 0.3293 | 0.4266 | 0.3051 | 0.2993 | 0.0968 |
| 1 | 365 | 50 | 0.1558 | 0.0990 | 0.1474 | 0.1913 | 0.1507 | 0.1634 | 0.1202 | 0.0917 | 0.1294 | 0.1388 | 0.0318 |
| 1 | 365 | 115 | 0.1877 | 0.3214 | 0.1353 | 0.1079 | 0.1445 | 0.1155 | 0.1393 | 0.1002 | 0.1527 | 0.1561 | 0.0673 |
| 1 | 3650 | 75 | 0.4292 | 0.1602 | - | 0.4672 | 0.1892 | 0.1886 | 0.2549 | 0.2410 | 0.4950 | 0.3032 | 0.1375 |
| 1 | 1000 | 115 | 0.2208 | 0.2216 | 0.2056 | 0.4155 | 0.1323 | 0.2119 | 0.1790 | 0.1612 | 0.1826 | 0.2145 | 0.0810 |
| 2 | 12 | 75 | 0.4615 | 0.2730 | 0.3807 | 0.3761 | 0.4918 | - | 0.4691 | 0.4427 | 0.5647 | 0.4325 | 0.0883 |
| 2 | 52 | 75 | 0.4829 | 0.4718 | 0.4978 | 0.5172 | 0.4758 | 0.4808 | 0.1828 | 0.2517 | 0.1681 | 0.3921 | 0.1458 |
| 2 | 365 | 75 | 0.1368 | 0.3281 | 0.3531 | 0.2802 | 0.2732 | - | 0.2832 | 0.1227 | 0.1225 | 0.2375 | 0.0951 |
| 2 | 1000 | 75 | 0.2463 | 0.4235 | 0.4593 | 0.2085 | 0.1123 | 0.3187 | 0.3264 | 0.0978 | 0.5188 | 0.3013 | 0.1487 |
| 2 | 365 | 20 | 0.2211 | 0.2402 | 0.2302 | 0.2914 | 0.1568 | 0.4792 | 0.3502 | 0.4167 | - | 0.2982 | 0.1092 |
| 2 | 365 | 50 | - | 0.4127 | 0.2370 | 0.2417 | 0.3939 | 0.2197 | 0.2911 | 0.2694 | 0.3118 | 0.2972 | 0.0721 |
| 2 | 365 | 115 | 0.1390 | 0.0976 | 0.0756 | 0.1465 | 0.2979 | 0.1751 | 0.2403 | 0.3862 | 0.4595 | 0.2242 | 0.1328 |
| 2 | 3650 | 75 | 0.3213 | 0.2589 | 0.2310 | 0.3195 | 0.1661 | 0.1278 | 0.2227 | 0.2482 | 0.2092 | 0.2339 | 0.0636 |
| 2 | 1000 | 115 | 0.0915 | 0.1963 | 0.2670 | 0.0812 | 0.1493 | 0.1230 | 0.1586 | 0.0819 | 0.0898 | 0.1376 | 0.0629 |

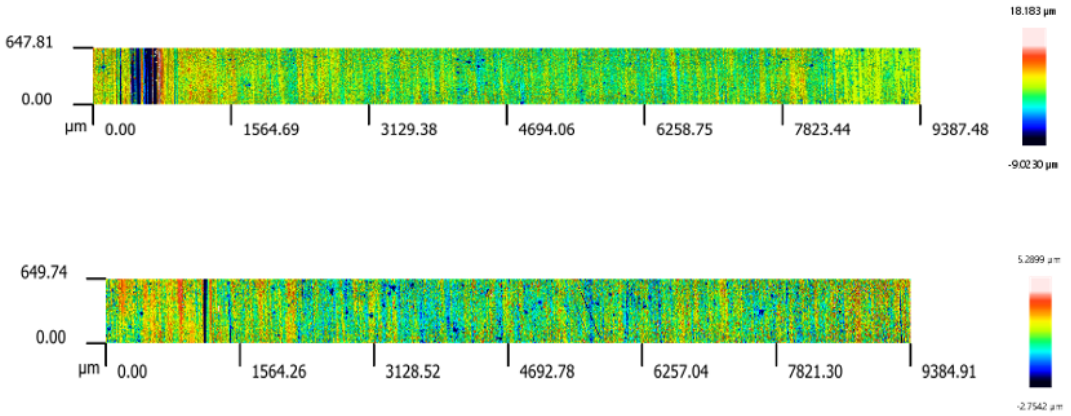


FIGURE .7: The confocal images of sample 1 of the silver coated plate for 365 number of strokes at 75 °C.

TABLE .3: Results of the silver coated plate after the wear test at stroke number 365

| Sample | Stroke | Temp °C | RaL $\mu$m | RaR$\mu$m | RqL$\mu$m | RqR$\mu$m |
|---|---|---|---|---|---|---|
| 1 | 365 | 20 | 0.5241 | 0.5881 | 0.60885 | 0.6792 |
| 1 | 365 | 50 | 0.3457 | 0.3365 | 0.37915 | 0.2768 |
| 1 | 365 | 75 | 0.3169 | 0.6513 | 0.27705 | 0.3145 |
| 1 | 365 | 115 | 0.3395 | 0.5327 | 0.4477 | 0.5057 |
| 2 | 365 | 20 | 0.71425 | 0.3897 | 0.8399 | 0.5104 |
| 2 | 365 | 50 | 0.3558 | 0.3148 | 0.4625 | 0.3975 |
| 2 | 365 | 75 | 0.5833 | 0.5033 | 0.7299 | 0.6343 |
| 2 | 365 | 115 | 0.39585 | 0.3087 | 0.509 | 0.3997 |

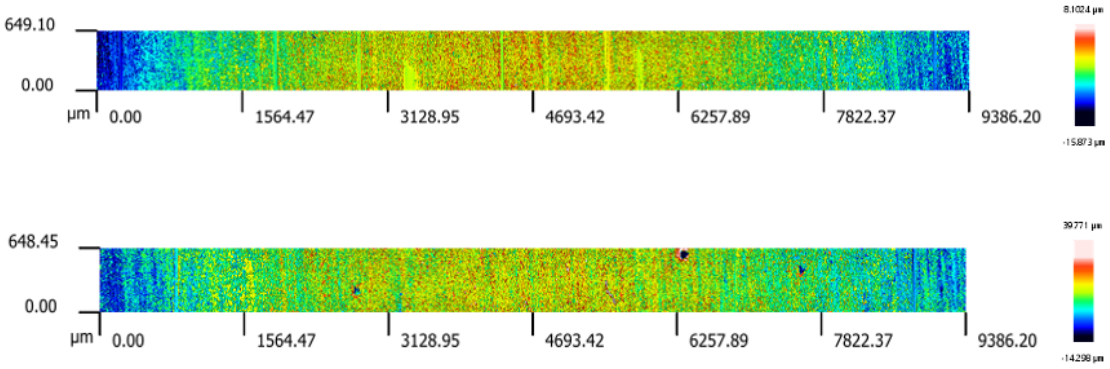


FIGURE .8: The confocal images of sample 2 of the silver coated plate for 365 number of strokes at 75 °C.